



Broad immune activation underlies shared set point signatures for vaccine responsiveness in healthy individuals and disease activity in patients with lupus

Yuri Kotliarov^{1,7,12}, Rachel Sparks^{2,12}, Andrew J. Martins², Matthew P. Mulè^{2,3}, Yong Lu², Meghali Goswami^{2,8}, Lela Kardava⁴, Romain Banchereau^{5,9}, Virginia Pascual^{5,10}, Angélique Biancotto^{1,11}, Jinguo Chen¹, Pamela L. Schwartzberg^{1,6}, Neha Bansal², Candace C. Liu², Foo Cheung¹, Susan Moir⁴ and John S. Tsang^{1,2}

Responses to vaccination and to diseases vary widely across individuals, which may be partly due to baseline immune variations. Identifying such baseline predictors of immune responses and their biological basis is of broad interest, given their potential importance for cancer immunotherapy, disease outcomes, vaccination and infection responses. Here we uncover baseline blood transcriptional signatures predictive of antibody responses to both influenza and yellow fever vaccinations in healthy subjects. These same signatures evaluated at clinical quiescence are correlated with disease activity in patients with systemic lupus erythematosus with plasmablast-associated flares. CITE-seq profiling of 82 surface proteins and transcriptomes of 53,201 single cells from healthy high and low influenza vaccination responders revealed that our signatures reflect the extent of activation in a plasmacytoid dendritic cell-type I IFN-T/B lymphocyte network. Our findings raise the prospect that modulating such immune baseline states may improve vaccine responsiveness and mitigate undesirable autoimmune disease activity.

The immune system maintains health but also contributes to diverse pathologies¹. The extent of immune responses to a perturbation or disease varies across individuals in the population, so there is a pressing need to uncover predictors and determinants of immune responsiveness in humans^{2–4}. Human immune responses are not only shaped by genetics but are also markedly influenced by the environment^{3,5,6}; for example, antibody responses to vaccination show little heritability after infancy or early childhood^{7,8}. Increasing evidence supports the hypothesis that the immune state of an individual before a perturbation can predict and determine immune response outcomes³. However, the molecular and cellular basis for the few existing baseline peripheral blood cell frequency or transcriptional predictors in humans^{9–12} remains largely unknown.

Some immunologic mechanisms that contribute to protective immune responses in vaccination and infection can mediate undesirable disease activity in patients suffering from an autoimmune disease. Notably, responses to influenza, yellow fever and many other vaccines and infections are characterized by a plasmablast increase detectable in blood³. A plasmablast increase has been shown to coincide with disease activity in some autoimmune patients, such as a subset of the patients with systemic lupus

erythematosus (SLE)¹³, a chronic, heterogeneous autoimmune disease that often presents clinically with episodic disease flares affecting multiple organs¹⁴. We thus hypothesized that there are common baseline determinants that contribute to the responsiveness to both vaccination/infection and autoimmunity in the form of undesirable disease activity. The determinants of disease activity, such as the intensity of flares in SLE, are poorly understood and predictors of such activity remain elusive¹⁵. Given the availability of longitudinal blood transcriptomic data in SLE¹³ and the relevance of plasmablasts in both vaccination/infection and SLE, we use SLE in the current study as a model for exploring common baseline signatures associated with vaccine responses in healthy individuals and autoimmune disease activity in patients.

We show that a baseline, temporally stable peripheral blood signature predictive of antibody responses to influenza vaccination¹² is also predictive of responses to the yellow fever vaccine in individuals naive to the virus. The same signature evaluated at clinical quiescence (baseline-like) is associated with disease activity in patients with SLE with flares characterized by an elevation in plasmablast signature scores (Fig. 1a). Conversely, a biologically related baseline indicator of disease flares derived solely from the same subset of patients with lupus is correlated with antibody responses to

¹NIH Center for Human Immunology, NIAID, NIH, Bethesda, MD, USA. ²Multiscale Systems Biology Section, Laboratory of Immune System Biology, NIAID, NIH, Bethesda, MD, USA. ³NIH-Oxford-Cambridge Scholars Program; Cambridge Institute for Medical Research and Department of Medicine, University of Cambridge, Cambridge, UK. ⁴B Cell Immunology Unit, Laboratory of Immunoregulation, NIAID, NIH, Bethesda, MD, USA. ⁵Baylor Institute for Immunology Research, Dallas, TX, USA. ⁶Cell Signaling and Immunity Section, Laboratory of Immune System Biology, NIAID, NIH, Bethesda, MD, USA. ⁷Present address: Biometric Research Program, Division of Cancer Treatment and Diagnosis, NCI, NIH, Rockville, MD, USA. ⁸Present address: Laboratory of Myeloid Malignancies, NHLBI, NIH, Bethesda, MD, USA. ⁹Present address: Oncology Biomarker Development, Genentech Inc., South San Francisco, CA, USA. ¹⁰Present address: Drukier Institute for Children's Health at Weill Cornell Medicine, New York, NY, USA. ¹¹Present address: Sanofi Precision Immunology, Immunology and Inflammation Therapeutic Area, Cambridge, MA, USA. ¹²These authors contributed equally: Yuri Kotliarov, Rachel Sparks. e-mail: john.tsang@nih.gov

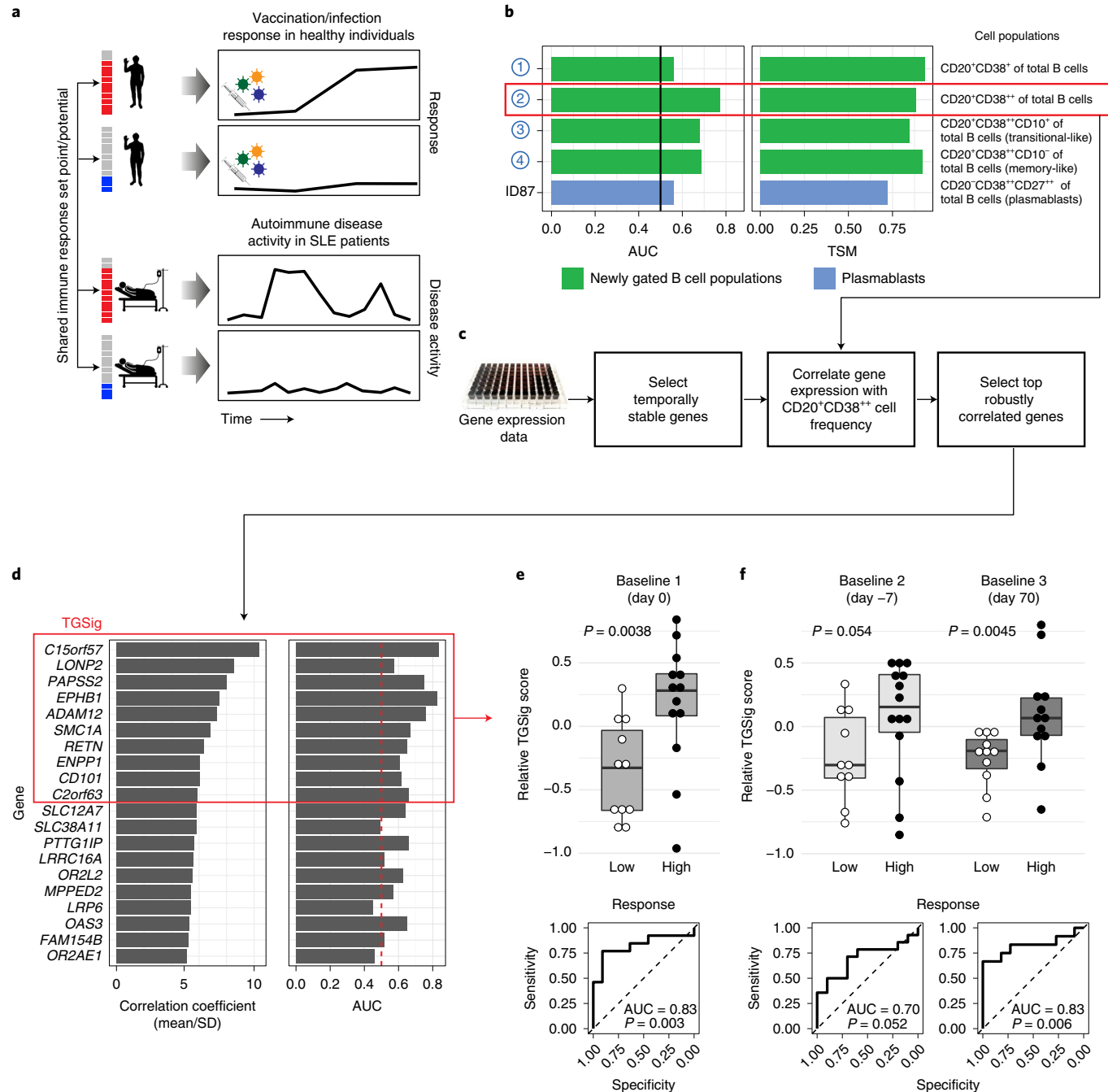


Fig. 1 | Study questions and the derivation of a baseline, pre-vaccination signature predictive of response using an influenza vaccination cohort.

a, Overview of the study and research questions. **b**, Prediction performance for antibody response in the NIH influenza study¹² using the frequency of several B cell subsets (y axis) (see Methods and gating strategy outlined in Extended Data Fig. 1a). The left panel shows the AUC (area under receiver operator curve; x axis) for predicting high and low responders ($n=23$ with flow cytometry data) to the seasonal and pandemic H1N1 influenza vaccines¹². The right panel shows the temporal stability metric (TSM) (x axis); higher TSM indicates greater temporal stability over the three baseline time points (days -7 and 0 prior to vaccination and day 70 after vaccination) using 136 samples from 51 subjects. Population 2 (red box) is the CD19⁺CD20⁺CD38⁺⁺ B cell population. **c**, Flow chart showing the steps to derive the gene expression based surrogate signature (TGSig). **d**, Top temporally stable genes correlated with the frequency of CD19⁺CD20⁺CD38⁺⁺ B cells and the selected genes in TGSig (red box). Twenty-two high and low responders (those with both gene expression and flow cytometry data) are used to assess correlations and rank genes. Genes are ranked based on the average Spearman correlation divided by the standard deviation obtained from 231 iterations (as a safeguard against noise we iterated over all sub-cohorts containing 20 subjects by taking out 2 random subjects at a time (that is, excluding 2 out of 22 subjects) to assess the correlation). See Extended Data Fig. 2a-d and Methods for further details about temporal stability, gene selection, and signature score calculation. **e**, Top: box plots comparing the TGSig score (y axis) at day 0 (pre-vaccination) between low ($n=11$) and high ($n=13$) responders (x axis) (Wilcoxon one-tailed P value shown); bottom: receiver operating curve (ROC) for assessing predictive capacity (AUC and one-tailed permutation test P value shown). Box plot centre lines correspond to the median value; lower and upper hinges correspond to the first and third quartiles (the 25th and 75th percentiles); and lower and upper whiskers extend from the box to the smallest or largest value correspondingly, but no further than 1.5× inter-quartile range. **f**, Similar to **e** but for the other two baseline time points: day -7 (10 low and 14 high responders) and day 70 (11 low and 12 high responders).

influenza vaccination in healthy subjects. We thus provide robust evidence for baseline ‘set point’² signatures shared among vaccinated healthy subjects and patients with SLE. Simultaneous protein and transcriptome analysis¹⁶ (CITE-seq; cellular indexing of transcriptomes and epitopes by sequencing) of single peripheral blood mononuclear cells (PBMCs) from healthy high and low responders of influenza vaccination revealed that our signatures reflect the extent of activation in multiple immune cell populations at baseline, including plasmacytoid dendritic cells (pDCs) and lymphocytes. These findings suggest that future responsiveness potential can be stably encoded by the activation status of a cellular network before perturbation and provide interventional targets that can potentially be modulated—at baseline and under homeostatic conditions—to improve human health.

Results

Development of a temporally stable transcriptional baseline signature predictive of antibody responses to influenza vaccination. We previously identified a baseline (pre-vaccination), temporally stable signature predictive of antibody responses to influenza vaccination independent of age, gender and pre-existing antibody levels¹². The signature consisted of the frequency of several B and T cell subpopulations without antigen-specific information. We subsequently noticed that all the predictive B cell populations expressed CD20 and high levels of CD38 (CD19⁺CD20⁺CD38⁺⁺), suggesting that these markers together defined a core predictive population (Extended Data Fig. 1a). We quantified this and related populations in the three baseline time points in our original NIH influenza vaccination study (days −7 and 0 prior to vaccination and day 70 when the parameters altered by vaccination had returned to their original values)^{12,17} (Fig. 1b). As expected, high and low antibody responders (defined using the ‘adjMFC’ metric that does not depend on pre-existing antibody levels against influenza¹²) could be distinguished by the frequency of the CD20⁺CD38⁺⁺ cells at all three time points (Extended Data Fig. 1b, c). As observed previously¹², this signature was independent of plasmablasts (CD20[−]CD38⁺⁺), which alone could not predict the response (AUC = 0.55; Fig. 1b).

To test whether our CD20⁺CD38⁺⁺ signature could predict immune responsiveness in other scenarios using independent datasets, we developed a blood-based transcriptional surrogate as available public datasets either do not have flow cytometry data or, if present, do not measure the same cell subsets. We identified

temporally stable genes robustly correlated with the frequency of CD20⁺CD38⁺⁺ cells across subjects on day 0 in the NIH cohort to build a 10-gene signature (TGSig, see Glossary in Extended Data Fig. 1d) (Fig. 1c–e, Extended Data Fig. 2a–f and Supplementary Table 1; see also Methods). TGSig has AUCs comparable to the frequency of CD20⁺CD38⁺⁺ B cells when evaluated in the other two baseline time points (Fig. 1f), and it was robust against removal of genes (Extended Data Fig. 2g). Similar and statistically significant trends were observed when middle responders were included (Extended Data Fig. 3a).

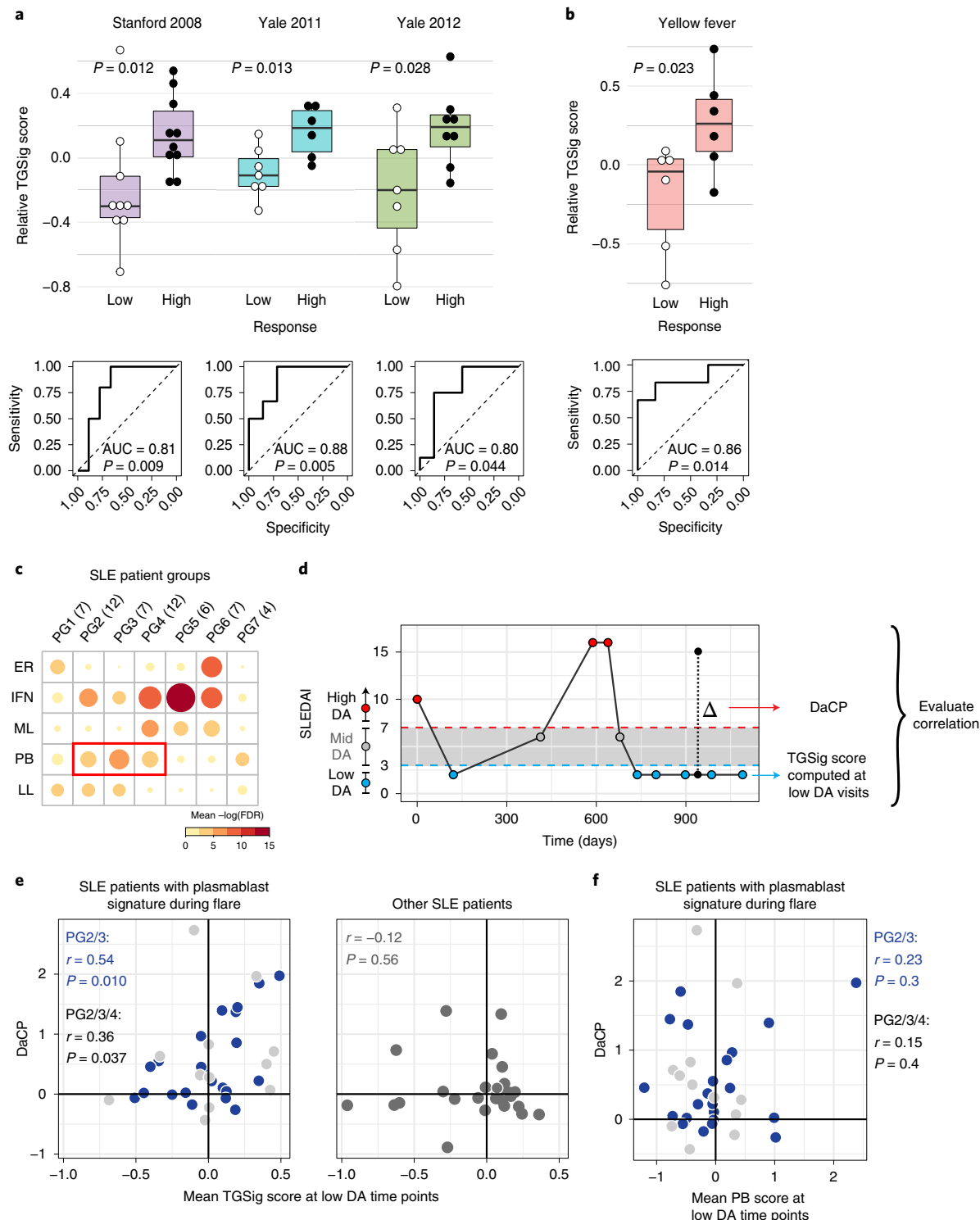
Evaluating TGSig in independent influenza and yellow fever vaccination datasets. We next assessed TGSig in independent influenza vaccination cohorts from multiple institutions. These data together with our NIH cohort span three geographic locations within the US and vaccination years (2008, 2009, 2011 and 2012)¹⁰ (Supplementary Table 2). Application of TGSig to the pre-vaccination, baseline data of multiple datasets without any further model training showed good prediction performance (AUCs > 0.8; $P < 0.05$ permutation test) (Fig. 2a; see also Extended Data Fig. 3b, which includes middle responders). However, it lacked predictive power when applied to influenza vaccination data from another US institution covering four consecutive vaccination years (2008–2011)¹⁸, which became available after our initial analyses (Extended Data Fig. 3c). While many technical or biological factors could be responsible for this result, we have ruled out differences in low-level data processing or high/low responder definition (see Methods).

We next investigated whether TGSig could predict responses to a live viral infection by using yellow fever vaccination (YF-17D) given to healthy adults naive to YF-17D as a model¹⁹. Unlike responses to the influenza (dead/inactivated) vaccine, YF-17D is a live, attenuated virus that would be expected to generate an antibody response through partially distinct immunological mechanisms. TGSig applied to pre-vaccination PBMC expression data was again able to separate high and low responders in the larger of two independent trials (Fig. 2b; AUC = 0.86, $P = 0.014$ permutation test; see also Extended Data Fig. 3d, which includes middle responders). A similar but not statistically significant trend was observed in a smaller second independent trial that had fewer subjects (4 high and 3 low responders; Extended Data Fig. 4a) (AUC = 0.75; $P = 0.11$ permutation test). A meta-analysis of the influenza vaccination datasets for which TGSig exhibited predictive capacity at

Fig. 2 | Assessing TGSig in independent influenza vaccination, yellow fever vaccination and SLE datasets. **a**, Same as Fig. 1e in terms of statistical tests and plot types, but here showing the predictive performance of TGSig (evaluated at baseline/pre-vaccination) in the indicated independent datasets: Stanford 2008 (purple boxes; 10 high versus 8 low responders), Yale 2011 (turquoise; 6 high versus 7 low responders) and Yale 2012 (green; 8 high versus 7 low responders) with the corresponding ROC shown at the bottom. **b**, Similar to **a** but for yellow fever vaccination. This cohort (trial 1) included 6 high and 6 low responders; see Extended Data Fig. 4a for results on a second, smaller cohort (trial 2) with 10 subjects (4 high and 3 low responders) from the same publication¹⁹. See also Extended Data Fig. 3d for box plots that include middle responders. **c**, SLE patient groups determined based on the blood gene expression signatures associated with disease activity/flare (see also Extended Data Fig. 5a and Methods). The color and size of the circle denote the average statistical significance ($-\log_{10}$ of BH (Benjamini-Hochberg)-adjusted P values from the CERNO test³⁹) of the association across patients in the group. The patient group IDs (columns) are listed with the number of patients in each group in parentheses. The same phenotypic annotations from ref. ¹³ are used: ER, erythropoiesis; IFN, IFN response/neutrophils; ML, myeloid lineage/neutrophils; PB, plasmablasts; LL, lymphoid lineage. The three groups with prominent PB signatures are boxed in red. **d**, Overview of the analysis approach. The dynamics of disease activity (DA) as measured by the SLE disease activity index (SLEDAI) score of an actual patient is shown. Individual visits are shown as dots (low disease activity (blue dots), SLEDAI < 3; medium disease activity (grey), SLEDAI = 3–7; high disease activity (red), SLEDAI ≥ 8). The TGSig score was computed from the low disease activity time points and the DaCP was computed from all time points using a mixed effect model accounting for treatment effects (see Methods); the correlation between TGSig (averaged across low disease activity time points) and DaCP was then evaluated. DaCP, disease-activity-associated change in plasmablast score. **e**, Scatterplot showing the relationship between the DaCP (y axis) and the mean TGSig score at low disease activity time points (x axis) in patient groups 2, 3 and 4 (34 subjects; left panel) and subjects whose disease activity tended not to be associated with a plasmablast signature (patient groups 1, 5, 6 and 7; 27 subjects; right panel). Pearson correlation coefficients and two-tailed P values are shown, and for the left panel separately for patient groups 2 and 3 only (blue dots, $n = 22$) or groups 2, 3 and 4 (blue and grey dots; $n = 34$). As a robustness check we also computed the Spearman correlation: rho = 0.47 ($P = 0.029$ two-tailed test) for groups 2 and 3; rho = 0.36 ($P = 0.038$ two-tailed test) for groups 2, 3 and 4; rho = −0.12 ($P = 0.56$ two-tailed test) for the rest of the patient groups. **f**, Same as in **e** but the plasmablast signature score was computed from the low disease activity time points instead of TGSig. Groups 2 and 3: Spearman rho = 0.014 ($P = 0.95$ two-tailed test); groups 2, 3 and 4: rho = −0.006 ($P = 0.97$ two-tailed test).

the individual cohort level (Stanford 2008, NIH 2009, Yale 2011, Yale 2012) indicated that genes in TGSig had positive ‘meta’ effect sizes and were thus positively associated with antibody responses (Extended Data Fig. 4b); the effect sizes were also qualitatively consistent with those in the yellow fever dataset (Extended Data Fig. 4c). Together, our data revealed that TGSig could predict the antibody response to a live attenuated virus in subjects naive to the virus and to the inactivated seasonal influenza vaccine in several, but not all, healthy cohorts tested.

Evaluating TGSig in SLE. We next assessed the hypothesis that TGSig evaluated at clinically quiescent periods of SLE patients (that is, low or no disease activity, resembling ‘baseline’) might also be associated with the severity of flares (Fig. 1a), which is dynamic and conceptually similar to responses following vaccination or infection. We analyzed a longitudinal paediatric SLE cohort¹³ in which the SLEDAI, a clinical assessment score that combines disease activity in several organs and clinical categories,¹³ was used to quantify disease activity over time. Previous analysis of this cohort identified



seven patient groups in which disease activity (that is, SLEDAI score) correlated with distinct combinations of blood transcriptomic signatures, including a module enriched for plasma cells/plasmablasts¹³ (Fig. 2c). We hypothesized that for patients whose disease activity was correlated with a plasma cell/plasmablast signature (Fig. 2c and Extended Data Fig. 5a; patient group (PG) 2 and PG3, and to a lesser extent, PG4), the disease-activity-associated change in plasmablast score (DaCP, see Extended Data Fig. 1d) between periods of low and high disease activity may be correlated with the TGSig evaluated at clinically quiescent periods (Fig. 2d).

We created a mixed-effects model to estimate the DaCP for PG2, PG3 and PG4 after accounting for treatments (see Methods). As expected, the DaCP values estimated by our procedure were correlated with the change in the average plasmablast score between low and high disease activity periods (Extended Data Fig. 5b). We detected a mild but significant correlation between the mean of TGSig across periods of low disease activity (SLEDAI < 3) and DaCP (Pearson $r=0.359$, $P=0.037$; Fig. 2e). This correlation was stronger in PG2 and PG3 only (Pearson $r=0.535$, $P=0.010$) because PG4 often had weaker plasmablast signals associated with disease activity (Extended Data Fig. 5a). To further evaluate this hypothesis, we tested the correlation when we removed patients whose DaCP was lower than a set threshold. We observed that the correlation tended to increase as the threshold increased (Extended Data Fig. 5c,d), confirming that the correlation between TGSig and DaCP was specific to those patients with plasmablast-associated flares. As a control, we performed the same analyses for patients who did not show a plasmablast signature (PG1, PG5, PG6 and PG7; Fig. 2c) and found no correlation (Pearson $r=-0.116$, $P=0.56$; Fig. 2e, right panel). We also confirmed that there was no correlation between the DaCP and the mean plasmablast score at low disease activity time points in PG2, PG3 and PG4 (Fig. 2f). Thus, the plasmablast signature evaluated at periods of low disease activity was not predictive and TGSig did not reflect plasmablast activity. These results suggest that for SLE patients whose disease activity was associated with a plasmablast signature, TGSig evaluated during clinical quiescence can inform the magnitude of disease flares. These findings also expand the predictive value of TGSig from response to vaccines and infections to that associated with flares in a specific subtype of SLE.

An independently derived baseline signature from SLE is associated with influenza vaccination responses. Our results suggest a biological parallel between vaccination/infection responses and lupus disease activity. We therefore examined whether an

independently derived correlate of DaCP in SLE patients alone may conversely associate with the magnitude of antibody responses to vaccination. We focused again on PG2, PG3 and PG4 (Fig. 2c) and used weighted gene co-expression network analysis (WGCNA)²⁰ to investigate whether there are temporally stable (across low disease activity time points) gene expression modules associated with DaCP (Fig. 3a, Supplementary Fig. 1a and Supplementary Table 3a; see also Methods). One module (the ‘brown’) was mildly correlated with the DaCP (Fig. 3b and Supplementary Fig. 1b; Pearson $r=0.31$, $P=0.04$ permutation test; full results in Supplementary Table 3b) but, intriguingly, it was enriched for type I IFN related blood transcription modules (BTMs)²¹ (Fig. 3c and Supplementary Fig. 1c), consistent with type I IFN signatures seen in many SLE patients²². Our observation suggests that the magnitude of a type I IFN signature during clinical quiescence may be prognostic of disease activity for patients exhibiting plasmablast-associated flares.

To assess whether the brown module was correlated with vaccination responses, we used the meta-analysis results of influenza cohorts above to maximize statistical power (Supplementary Table 4a) and found that the brown module was significantly enriched for genes associated with antibody responses ($P=0.01$, GSEA test; Fig. 3d and Supplementary Table 4b). However, this was not the case for the yellow fever dataset (data not shown), perhaps due to the small cohort size and thus insufficient statistical power. Together, these observations provide independent support to our TGSig finding above that shared baseline signatures can exist for influenza vaccination responses and SLE disease activity.

Both baseline signatures are associated with type I IFN responses and activation of dendritic cells. Given their qualitatively similar predictive profiles, TGSig and the brown module might reflect overlapping biology, even though they shared only one gene (*EPHB1*) from the 370 genes in the brown module. Since TGSig was derived from the temporally stable genes most robustly correlated with the frequency of CD20⁺CD38⁺⁺ B cells (Fig. 1d), we ranked the temporally stable genes by their correlation with the frequency of these B cells and found that the most correlated genes were enriched for the brown module as well as type I IFN and dendritic cell (DC) activation related BTMs (Fig. 3e; see Methods). These results established functional links between the brown module and TGSig, and suggest that they reflect aspects of the type I IFN response/DC activation pathway. To capture the biology of this overlap for further analysis, we created the IFN-I-DCact (type I IFN and DC activation; see Extended Data Fig. 1d) gene signature comprising genes in the

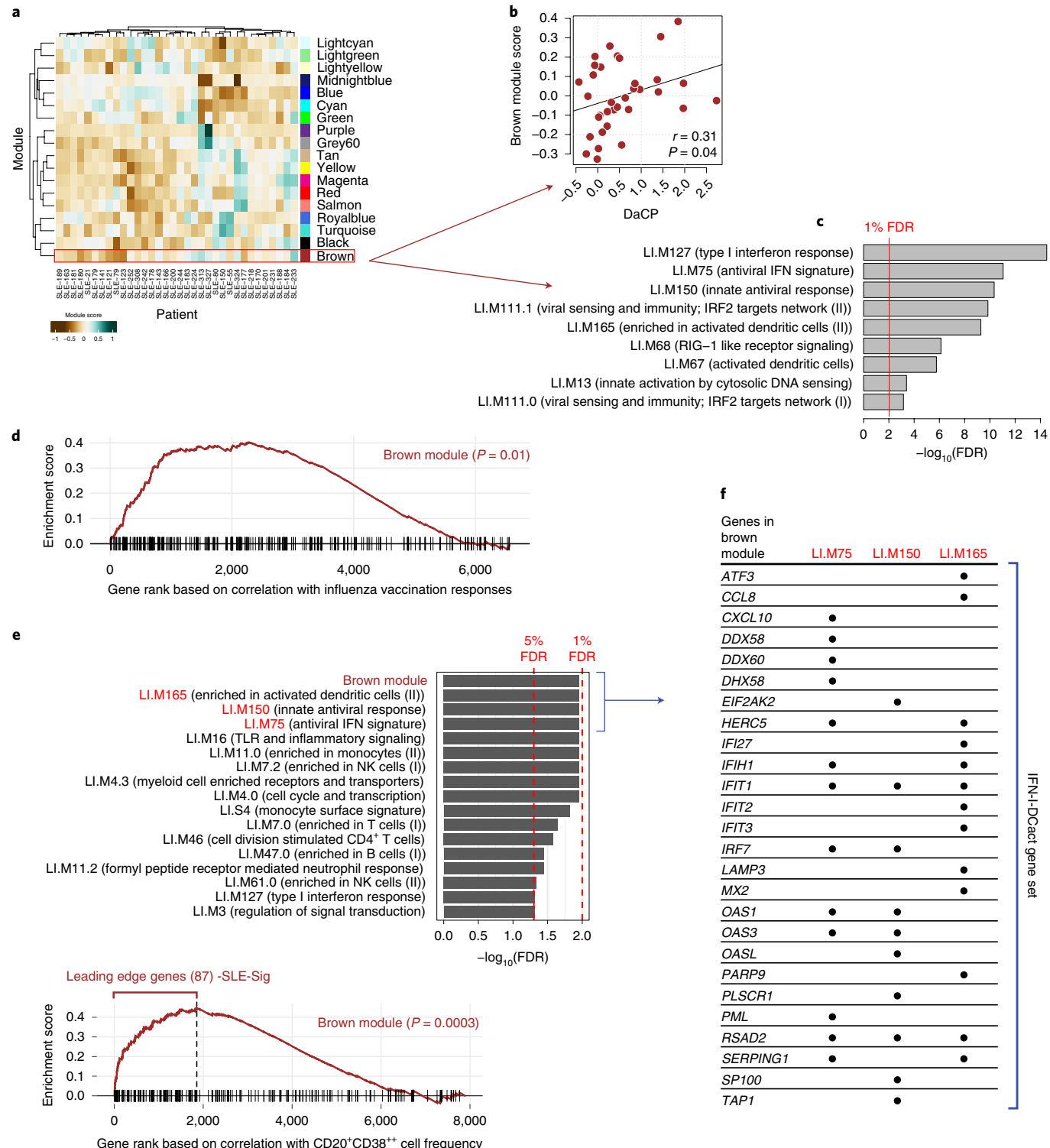
Fig. 3 | A transcriptional correlate of plasmablast-associated disease activity in SLE is also associated with influenza vaccination responses and functionally related to TGSig. **a**, Identification of 18 transcriptomic modules from genes whose expression was temporally stable across low disease activity time points in SLE patients from patient groups 2, 3 and 4. The heatmap shows the eigengene of each module averaged across low disease activity time points of each patient. Rows and columns correspond to modules and SLE patients, respectively. The number of genes in each module is shown in Supplementary Fig. 1a. **b**, Scatterplot showing the relationship between the brown module score and the DaCP for patients in groups 2, 3 and 4 as above ($n=34$; Pearson correlation = 0.31, $P=0.04$ based on a one-tailed permutation test (Supplementary Fig. 1b)). Spearman rho = 0.29 ($P=0.05$ one-tailed permutation test). **c**, Top enriched blood transcription modules²¹ (BTMs) of the brown module (370 genes) based on the hypergeometric test with BH-adjusted Pvalues (FDR) shown; the red line corresponds to 1% FDR (no additional BTMs were identified at 5% FDR cutoff). Complete results of the enrichment analysis can be found in Supplementary Fig. 1c. **d**, Gene set enrichment analysis (GSEA) of the brown module genes (370 genes). 6,563 genes were ranked by their magnitude of association with antibody responses based on a meta-analysis of four influenza vaccination datasets (the enrichment P value shown was computed from the GSEA test⁴⁰). The tick marks denote the location of the genes in the brown module. **e**, Top: enrichment analysis of blood transcription modules and the brown module in the temporally stable genes from the NIH influenza study as ranked by their correlation with the frequency of CD20⁺CD38⁺⁺ B cells. A temporal stability score (see Methods) cutoff of 0.5 is used here to define 7,889 stable genes; the enrichment results are robust to the threshold used. 5% and 1% FDR are indicated by the red dashed lines (BH-adjusted Pvalues shown were computed from the GSEA test). Bottom: GSEA enrichment plot for the brown module. The top 87 genes in the brown module (based on the gene rank on the x-axis) were identified by GSEA as the ‘leading edge genes’ (that is, the main driver of the enrichment signal) (we called this gene set SLE-Sig). The P value shown was computed from the GSEA test. The full list of leading-edge genes can be found in Supplementary Table 5. **f**, Genes in the brown module that are also in at least one of the three top type I IFN/antiviral/dendritic cell activation BTMs from **e**; black dots indicate that the gene is present in the indicated gene set. These genes constitute the IFN-I-DCact gene set/signature reflective of type I IFN and DC activation.

brown module that are shared with at least one of the IFN-I/antiviral/DC activation BTMs (Fig. 3f).

We also evaluated the overlap among TGSig, SLE-Sig and IFN-I-DCact from a predictive standpoint by using data pooled from the meta-analysis above (see Methods). As expected, each signature on its own contained predictive information (Extended Data Fig. 6a–c), and most of the predictive capacity of the brown module came from the 87 ‘leading edge’ genes (SLE-Sig, see Extended Data Fig. 1d; see also Fig. 3e, Supplementary Table 5, Extended Data

Fig. 6d). When TGSig was used together with SLE-Sig or IFN-I-DCact for prediction, TGSig was the dominant predictor (Extended Data Fig. 6e,f). The same was true for predicting DaCP in the SLE cohort (data not shown). Thus, TGSig, as a baseline signature, contains most of the predictive information in SLE-Sig and IFN-I-DCact for both influenza vaccination and SLE disease activity.

CITE-seq analysis of high and low influenza vaccination responders to uncover the cellular origin of baseline signatures. To dissect



the cellular origin of our signatures, we sorted CD19⁺CD20⁺CD38⁺⁺ B cells from six healthy donors followed by RNA-seq (Extended Data Fig. 7a,b). However, genes differentially expressed in these cells compared to CD19⁺CD20⁺ B cells were not enriched for TGSig or SLE-Sig (Extended Data Fig. 7b–e), suggesting that neither originate from these cells.

Given the large number of possible cellular origins for TGSig and SLE-Sig, we pursued an unbiased approach by adopting CITE-seq¹⁶ to simultaneously profile 82 surface proteins (covering lineage and phenotypic markers of diverse immune cells) and the transcriptomes of 53,201 single cells from the baseline (day 0/pre-vaccination) PBMC of 10 high and 10 low responders from the NIH cohort (Fig. 4a; average 2,660 (SD = 753) cells per donor). A major goal was to assess whether our baseline signatures reflect transcriptional state differences between the high and low responders in certain cell subsets.

We clustered the cells²³ at several resolutions using their surface protein expression profile to reveal major cell types and subsets (Fig. 4a–c and Extended Data Fig. 8a–c; see Methods). The frequency of most cell clusters was not significantly associated with vaccination responses, except, for example, negative associations involving effector CD4⁺ memory (cluster C1.1.0) (data not shown), which is consistent with the original study (ID36 in Fig. 6c in ref. ¹²). TGSig computed using the ‘pseudo bulk’ data (averaged across all single cells for each subject; see Methods) was significantly higher in the high than the low responders (Fig. 4d). The same holds for SLE-Sig (Fig. 4e) and the frequency of manually gated CD20⁺CD38⁺⁺ B cells using CITE-seq data (Extended Data Fig. 8d,e; $P=0.032$ Wilcoxon one-tailed test). Thus, CITE-seq data reproduced our earlier findings from microarray and flow cytometric measurements.

We next evaluated TGSig and SLE-Sig differences between high and low responders within cell clusters (Supplementary Tables 6 and 7). Significant differences in the average expression of TGSig genes were found in pDCs (cluster C9), a major producer of type I IFNs and other cytokines²⁴ (Fig. 5a). SLE-Sig (Fig. 5b) was elevated broadly across cells clusters, including CD4⁺ central memory and CD8⁺ naive T cells (C1 and C6), classical monocytes and myeloid DCs (mDCs) (C2), transitional B cells (C3.0.0), and unconventional T cells (C7) (Fig. 5b). While the other clusters were not statistically significant, SLE-Sig trended higher in the high responders, suggesting that most peripheral immune cells were broadly exposed to higher levels of IFNs in high responders at baseline. Similar results were obtained using an independently derived type I IFN response gene set (Extended Data Fig. 8f and Supplementary Tables 6 and 7; see Methods).

Given that pDCs are major producers of type I IFN²⁴, the elevated type I IFN status in high responder cells from diverse lineages may be due to the presence of more activated pDCs in these individuals; we indeed found that the average expression of the genes in LI.M165 and IFN-I-DCact—both reflective of DC activation and

linked to TGSig and SLE-Sig (Fig. 3e,f)—was significantly elevated in pDCs of high responders (Fig. 5c).

Activated pDCs are known to activate T cells that then stimulate B cells via CD40L^{24,25}. To test whether we can detect the activation status of this circuit even at baseline, we derived a CD40 activation gene signature (CD40act; see Extended Data Fig. 1d) (Supplementary Table 6) from two independent studies of human B cells stimulated with CD40L^{26,27} (see Methods). CD40act was highly enriched for cell cycle processes (Fig. 5d), probably because CD40L-activated B cells are highly proliferative²⁸. As hypothesized, CD40act was significantly increased in switched B cells (C3.1.0) in high responders (Fig. 5e). It was also elevated significantly in several lymphocyte clusters (see Fig. 4b,c and Extended Data Fig. 8a,c for cell cluster annotations), including CD4⁺ memory (C1.0.0), CD8⁺ naive (C6) and unconventional CD161⁺ T cells (C7.0.0) (Fig. 5e). Together, these observations suggest that in high responders, the increased activation of pDCs and elevation of type I IFNs led to the activation and proliferation of not only switched B cells, but also T lymphocytes. Furthermore, we hypothesized and indeed observed that CD40 activation status in switched B cells (C3.1.0) was correlated with the frequency of CD20⁺CD38⁺⁺ B cells measured by flow cytometry (Fig. 5f). This suggests that the CD20⁺CD38⁺⁺ cells, our original baseline signature (Fig. 1b and Extended Data Fig. 1a,b), overlapped with activated switched B cells.

TGSig captures the activation/cell cycle and type I IFN response statuses of lymphocytes and myeloid cells. We next analyzed the correlation among the signatures, including TGSig assessed in ‘bulk’/PBMCs (Fig. 1c–e), the frequency of CD20⁺CD38⁺⁺ B cells (Extended Data Fig. 1b), and the significant cell-cluster-based signatures emerged from CITE-seq analysis (Fig. 6a). TGSig correlated with and thus captured the status of several signatures at the cell cluster level that delineated high versus low responders as determined by CITE-seq (left scatterplots in Fig. 6a). These signatures include both the activation/proliferation (as reflected by CD40act) and the type I IFN response statuses (as indicated by SLE-Sig) of switched B cell and several T cell clusters, and albeit more mildly, those of pDCs and mDCs. SLE-Sig (in PBMCs, as measured by microarrays) also captured the type I IFN response status of both lymphocytes and myeloid cells. However, SLE-Sig captured less well the activation/cell cycle status of switched B cells (C3.1.0) and T cell subsets (C1.0.0 and C6) (Fig. 6a), which were some of the most significant correlates of the response as revealed by CITE-seq (Fig. 5e).

Our single cell data gave us an opportunity to drop specific combinations of cell clusters from the data, and then evaluate whether the signature scores computed from the remaining cells are still associated with the response (Extended Data Fig. 8g). Consistent with the observations above, this analysis revealed that TGSig became uninformative of the response when both the CD4⁺ memory and CD8⁺ naive T cell clusters (C1 and C6) were dropped;

Fig. 4 | CITE-seq (simultaneous protein and transcriptome expression profiling in single cells) analysis of high and low influenza vaccine responders.

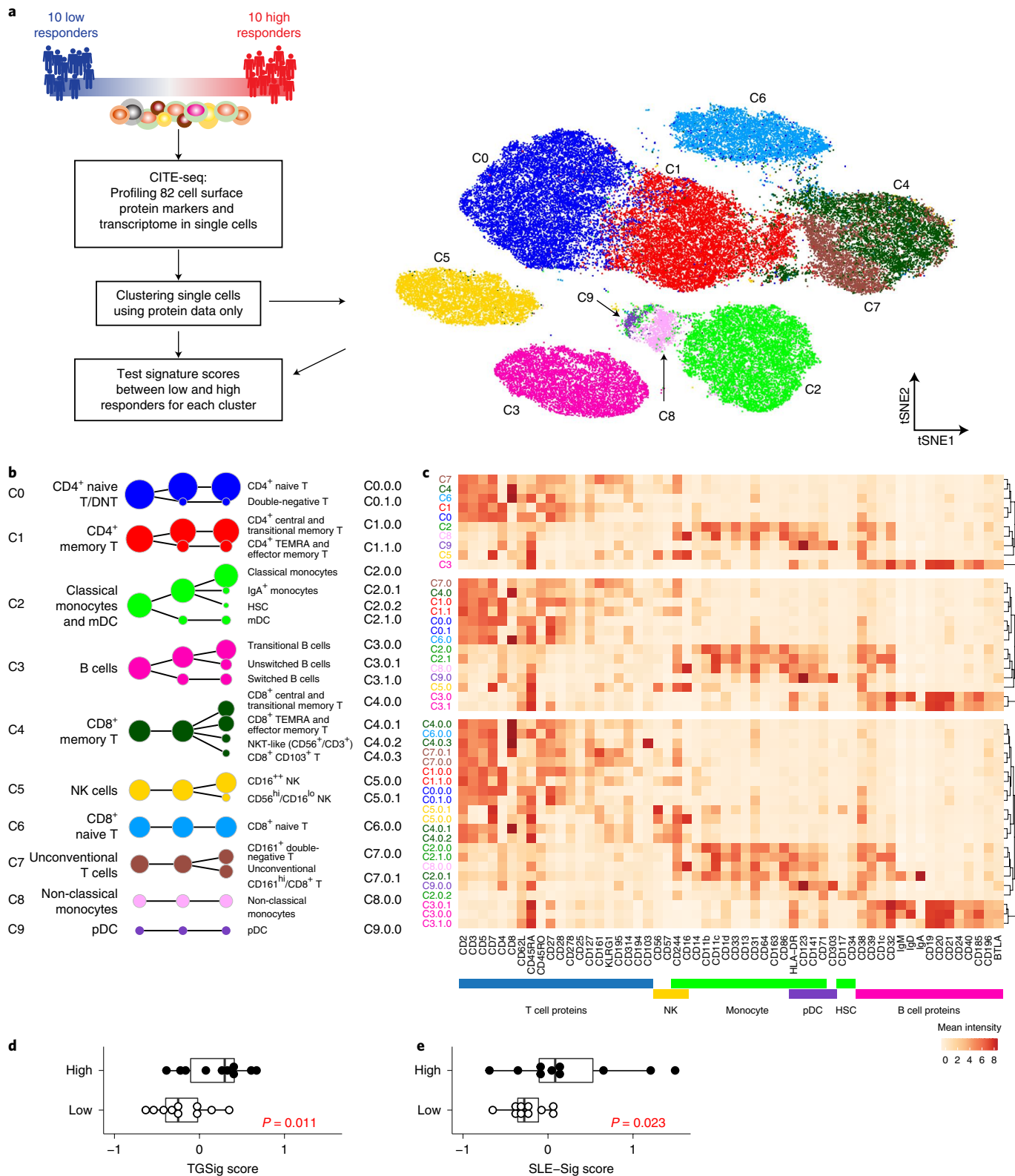
a, Experiment and analysis overview: single PBMCs from 10 high (red) and 10 low (blue) responders (as defined by adjMFC previously¹²) were profiled by CITE-seq (measuring 82 cell surface proteins and transcriptome). Cells from all subjects were clustered together using only surface protein expression profile at three increasingly detailed clustering resolutions (referred herein as levels 1–3, denoting the lowest to the highest resolutions; see Methods). Ten cell clusters (C0–C9) were identified at level 1 and shown in different colors in the tSNE plot. **b**, Cell clusters from levels 1–3 are shown in three columns and depicted as circles (size is proportional to the number of cells in the cluster). The edges denote containment relationship between the clusters at neighbouring resolutions: an edge connecting one cluster to another cluster indicates that some fraction (or all) of the cells in the former are found in the latter. Annotations are provided for levels 1 (first column) and 3 (third column) clusters. The clusters/circles are colored, matching those in the tSNE visualization. **c**, A heatmap showing the average expression of selected protein markers (columns) in each of the cell clusters (rows) derived from the three different clustering resolutions. The cell cluster names are color matched with those in **b**. See Extended Data Fig. 8a–c and Supplementary Fig. 2 for additional details. **d**, Box plot comparing the TGSig score between high (filled dot; $n=10$) and low (open dot; $n=10$) responders using ‘pseudo bulk’ data (average across all single cells within each subject; see Methods); P value from Wilcoxon one-tailed test. Box plot centre lines correspond to the median value; lower and upper hinges correspond to the first and third quartiles (the 25th and 75th percentiles); and lower and upper whiskers extend from the box to the smallest or largest value correspondingly, but no further than 1.5× inter-quartile range. **e**, Same as **d** but for SLE-Sig.

for SLE-Sig, the most important predictive information originated from the monocyte/mDC (C2) and CD4⁺ memory clusters (C1). Together, these observations suggest that even though TGSig only contains a few genes that were originally derived based on correlations with the frequency of the CD20⁺CD38⁺⁺ B cell population, it captures the responsiveness-predicting states of multiple cell subsets

in peripheral blood, particularly those of two subpopulations of Tlymphocytes that represent a substantial fraction of cells in blood.

Discussion

To our knowledge, predictors of autoimmune disease activity, particularly from clinically quiescent periods, are rare^{29,30}, and baseline



set point² signatures shared among vaccination, infection and an autoimmune disease have not been reported. Our simultaneous deep immunophenotyping and transcriptome analysis of single cells suggests that these predictive signatures reflect the extent of cell cycle/activation and type I IFN response statuses in a circuit comprising pDCs, switched B cells and T lymphocytes (Fig. 6b), thus pointing to a shared origin for our two independently derived but biologically related set point signatures. The sustained activation of these and related circuits have been implicated in the pathogenesis of SLE and other autoimmune diseases³¹, but here we provide fresh evidence that the elevated activation status of cells in this circuit during clinically quiescent periods in a subset of patients with SLE may indicate higher plasmablast-associated disease activity. Intriguingly, this circuit was also more activated in certain healthy subjects stably over the course of months, and these individuals tended to mount higher antibody responses to influenza or yellow fever vaccination. Thus, the future responsiveness potential to a perturbation can be encoded by the sustained activation status of a circuit that is typically fully activated only after an immune challenge (such as an infection). The mechanisms that restrain full-blown systemic immune activation before antigenic and inflammatory stimulation (particularly in healthy individuals) and the antigen-specific repertoire of the activated lymphocytes at baseline remained to be dissected (Fig. 6b).

Through CITE-seq analysis we found that the CD20⁺CD38⁺⁺ B cells we identified originally are likely to overlap with activated switched B cells, some of which could also be precursors of plasmablasts³². It is unlikely that all of these cells were influenza specific or persistently activated by influenza at baseline and remained temporally stable over months. They could be enriched with influenza specific cells in some individuals, but the fact that TGSig could predict responses in yellow fever naive subjects (Fig. 2b) suggests that TGSig does not simply reflect the frequencies of memory lymphocytes specific for particular vaccine antigens—unless this was all due to cross-reactivity, which is also unlikely. Furthermore, previous analysis of antigen-specific B cells¹² in the NIH cohort showed that baseline vaccine reactivity did not correlate with antibody responses, which was consistent with independent observations³³ that the frequency of pre-existing influenza-specific B cells in peripheral blood does not correlate with antibody responses following vaccination. Similarly, higher frequencies of activated, influenza-specific CD4⁺ T cells in peripheral blood at baseline were not positively associated with T cell responses following influenza vaccination³⁴.

Plasmacytoid DCs were probably a major source of type I IFNs that led to the elevated IFN response status across multiple cell lineages in the high responders (Fig. 5b and Extended Data Fig. 8f). Since they represent only a small fraction of circulating immune cells, TGSig and SLE-Sig are likely to reflect less on the activation

status of the pDCs but instead capture the downstream effects of pDCs on lymphocytes and monocytes, which are much more abundant in blood. Together, these results also illustrate how deep single cell analysis in human subjects with distinct responsiveness phenotypes can help unmask cellular origins and provide mechanistic hypotheses on bulk blood transcriptomic biomarkers.

It remains to be determined why pDCs in healthy high responders were more activated—persistent triggers of TLR7/9 could be involved²⁴. The microbiome could be responsible but seemed to largely affect naïve than recall responses based on a recent study in influenza vaccination⁶. Cytomegalovirus (CMV) status is possible but less likely because a known correlate, the frequency of TEMRA cells³⁵, was not significantly associated with responder class in our cohort (Extended Data Fig. 9a,b). While genetics could play a role, twin studies have indicated that antibody responses to influenza vaccination exhibit little heritability in adults⁷. Two relevant pDC phenotypes (HLA-DR and CD86 expression on pDCs (cluster C9))³⁵ with strong genetic drivers were not significantly different between high and low responders (Extended Data Fig. 9c). Similarly, none of the genes in TGSig was associated with any trans expression quantitative trait loci based on a large-scale study of the genetics of blood gene expression in healthy subjects³⁶. Age was not associated with TGSig in the NIH cohort (data not shown), but females tended to have higher TGSig scores than males (Extended Data Fig. 10a–c), which is consistent with earlier observation that females tend to mount higher responses to some vaccines but are more prone to autoimmunity³⁷. Intriguingly, however, even within each sex, TGSig could predict responsiveness (Extended Data Fig. 10d,e), again suggesting that TGSig is a general baseline predictor.

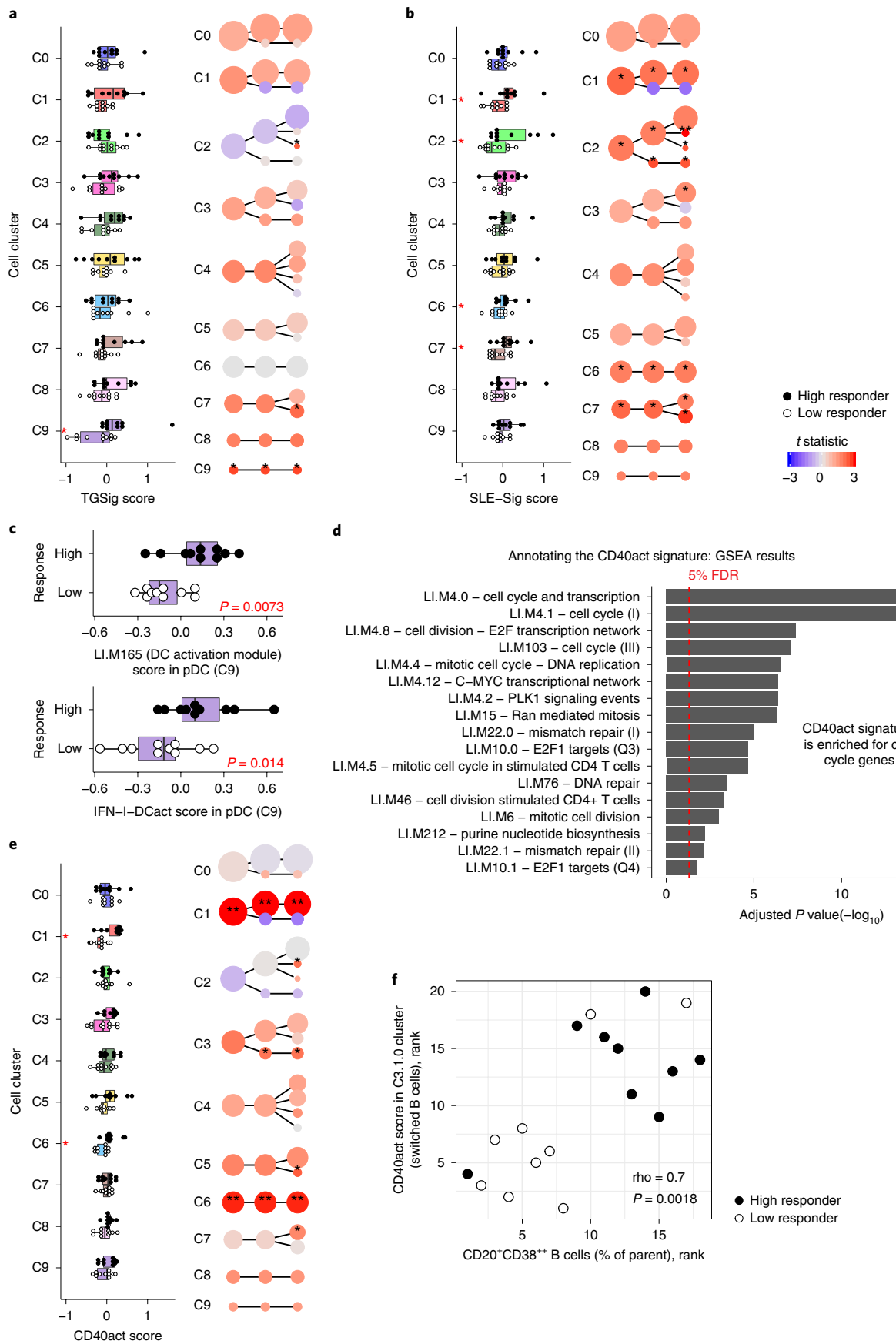
While TGSig's applicability in influenza (across three out of four US locations and over four different years), yellow fever and SLE supports the notion that it reflects common baseline determinants shared by these immune response scenarios, it was not predictive in influenza datasets from a US location over four consecutive years. It also remains to be determined whether it is applicable to other situations such as cancer immunotherapy and additional autoimmune diseases with flares associated with plasmablasts. TGSig was specific to a defined subtype of lupus as we had hypothesized (Fig. 2e), and all of the vaccination cohorts tested largely consisted of younger adults (aged under 45 years). In general, baseline set point signatures are probably not universally applicable but depend on factors such as age, ethnic background and geographic location^{10,38}. Rigorous clinical trials are ultimately needed to assess the applicability of these baseline signatures for different immune perturbations and diseases.

Given the centrality of the immune system in health and disease, our findings point to the prospect for longitudinal immune health assessment and monitoring as well as predicting future responses

Fig. 5 | Dissecting the cellular origin of baseline signatures. **a**, Evaluating the difference in TGSig score between high ($n=10$) and low ($n=10$) responders in each cell cluster from Fig. 4b (see Methods). Left: box plot comparing high (filled dot) and low (open dot) responders in each of the level 1 clusters (first column); each dot corresponds to the signature score of a subject. Red asterisks denote significance with $P < 0.05$ (Wilcoxon one-tailed test; see also Supplementary Table 7). The right panel uses the same visualization as in Fig. 4b, but here the color reflects the average normalized difference in TGSig signature score between the high and low responders (shown here as a t statistic). * $P < 0.05$ and ** $P < 0.01$ (Wilcoxon one-tailed test because we are interested in assessing whether the high responders are higher than the low responders; see also Supplementary Table 7). For all box plots the centre line corresponds to the median value, lower and upper hinges correspond to the first and third quartiles (the 25th and 75th percentiles), and lower and upper whiskers extend from the box to the smallest or largest value correspondingly, but no further than 1.5x inter-quartile range. **b**, Same as **a** but for SLE-Sig. **c**, Similar to the box plots in the left panel of **a** (10 high versus 10 low responders) but for the signature score of the LI.M165 BTM (top panel: enriched for dendritic cell activation) and the IFN-I-DCact (bottom panel; see Fig. 3f) gene sets evaluated for cells in the pDC cluster only (cluster C9). **d**, Enrichment analysis result of the CD40act gene set (Supplementary Table 6; 49 genes) using the hypergeometric test against the BTMs from ref. ²¹. All 32,738 detected genes were used as a background. BTMs with an adjusted one-tailed P value (FDR computed using the BH method) of 0.05 (red line) or lower are shown. **e**, Same as **a** but for CD40act. **f**, Scatterplot (based on ranks, since Spearman correlation is being evaluated) assessing the correlation between the frequency of CD20⁺CD38⁺⁺ B cells (see Fig. 1b) and the CD40 activation signature score in the switched B cell cluster (C3.1.0; see Fig. 4b,c). Spearman correlation and two-tailed P value are shown (based on 9 high and 9 low responders because not all 20 subjects assessed by CITE-seq have corresponding flow cytometry data). Detailed test statistics for data shown in **a,b,e** can be found in Supplementary Table 7.

to vaccination, infection and other perturbations using just a few markers in blood. Set point signatures could also be used to stratify populations in clinical trials and for properly accounting for

baseline heterogeneity when analyzing trial outcomes. Our results motivate the search for additional shared baseline determinants and predictive signatures among vaccination, infection, cancer, and



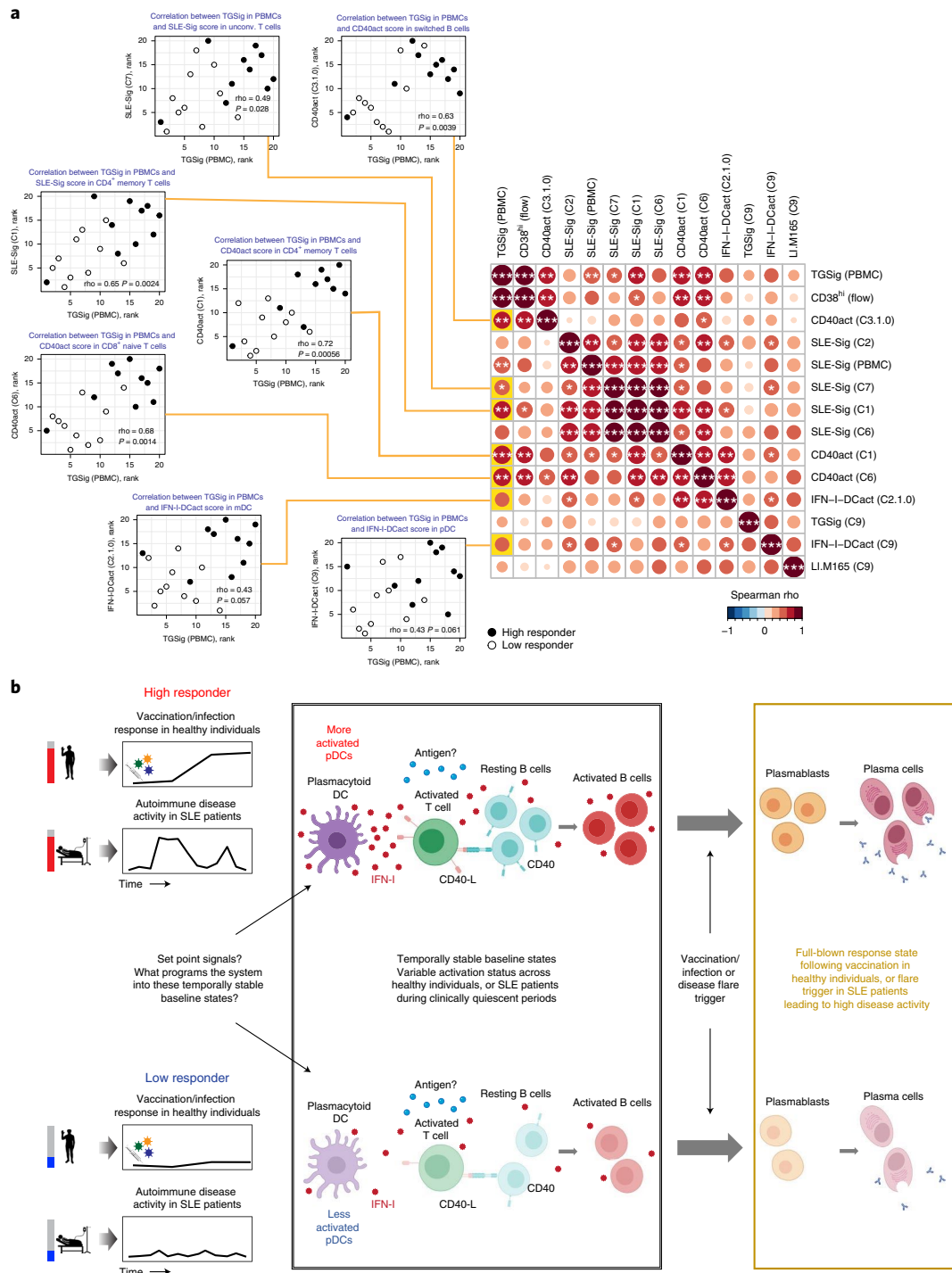


Fig. 6 | The correlative relationship among the single-cell-cluster-based and bulk (PBMC) signatures and a proposed cellular circuit whose pre-perturbation status determines future responsiveness. **a**, Matrix heatmap showing the pairwise Spearman correlation between the select signature scores across subjects. Example scatterplots similar to the one in Fig. 5f are shown for assessing the correlation between the original TGSig (computed using microarray data generated from PBMCs; see Fig. 1c–e) and the cell cluster based signature scores found to be significantly different between high ($n=10$) and low ($n=10$) responders. Spearman correlation and two-tailed P value are shown. The name of the cell cluster (see Fig. 4b,c) for which the indicated signature score was computed is in parentheses. Each example scatterplot corresponds to a highlighted (yellow) entry in the matrix on the right. The matrix is symmetrical: row and column profiles are identical. The size and shade of the circle indicate the correlation strength (Spearman rho) and asterisks denote significance level (two-tailed test) as shown in legend below. Note that SLE-Sig (PBMC) was computed using the original bulk microarray data (the same as TGSig (PBMC)). **b**, Model describing the molecular/cellular underpinnings and differences between high versus low responders. Activation of this entire circuit (including the components in the plasmablast/plasma cell box on the right) typically follows infection, vaccination, or occurs during autoimmune disease flares. Here we propose that the high responders tend to have more activated pDCs and thus more Type I IFNs and activated B and T cells at baseline, but only upon additional antigenic and/or inflammatory co-stimulation (and flare trigger in the case of SLE patients) does the system mount a full-blown plasmablast/plasma cell response cumulating in the generation of antibodies. Open questions include: 1) What sets the system into such temporally stable ‘activated’ states in pDCs, lymphocytes, and other myeloid cells? 2) What constrains the activated immune baselines from mounting full-blown plasmablast/plasma cell responses? 3) What is the antigen specificity repertoire of the activated lymphocytes at baseline?

autoimmune and inflammatory diseases, which may reveal new biology including common mechanisms underpinning different types of immune responses.

Online content

Any methods, additional references, Nature Research reporting summaries, source data, extended data, supplementary information, acknowledgements, peer review information; details of author contributions and competing interests; and statements of data and code availability are available at <https://doi.org/10.1038/s41591-020-0769-8>.

Received: 8 November 2019; Accepted: 14 January 2020;

Published online: 24 February 2020

References

- Kotas, M. E. & Medzhitov, R. Homeostasis, inflammation, and disease susceptibility. *Cell* **160**, 816–827 (2015).
- Chen, D. S. & Mellman, I. Elements of cancer immunity and the cancer-immune set point. *Nature* **541**, 321–330 (2017).
- Tsang, J. S. Utilizing population variation, vaccination, and systems biology to study human immunology. *Trends Immunol.* **36**, 479–493 (2015).
- Willis, J. C. D. & Lord, G. M. Immune biomarkers: the promises and pitfalls of personalized medicine. *Nat. Rev. Immunol.* **15**, 323 (2015).
- Brodin, P. & Davis, M. M. Human immune system variation. *Nat. Rev. Immunol.* **17**, 21–29 (2017).
- Hagan, T. et al. Antibiotics-driven gut microbiome perturbation alters immunity to vaccines in humans. *Cell* **178**, 1313–1328.e13 (2019).
- Brodin, P. et al. Variation in the human immune system is largely driven by non-heritable influences. *Cell* **160**, 37–47 (2015).
- Marchant, A. et al. Predominant influence of environmental determinants on the persistence and avidity maturation of antibody responses to vaccines in infants. *J. Infect. Dis.* **193**, 1598–1605 (2006).
- Krieg, C. et al. High-dimensional single-cell analysis predicts response to anti-PD-1 immunotherapy. *Nat. Med.* **24**, 144 (2018).
- HIPC-CHI Signatures Project Team & HIPC-I Consortium. Multicohort analysis reveals baseline transcriptional predictors of influenza vaccination responses. *Sci. Immunol.* **2**, eaal4656 (2017).
- Fourati, S. et al. Pre-vaccination inflammation and B-cell signalling predict age-related hyporesponse to hepatitis B vaccination. *Nat. Commun.* **7**, 10369 (2016).
- Tsang, J. S. et al. Global analyses of human immune variation reveal baseline predictors of postvaccination responses. *Cell* **157**, 499–513 (2014).
- Banchereau, R. et al. Personalized immunomonitoring uncovers molecular networks that stratify lupus patients. *Cell* **165**, 551–565 (2016).
- Tsokos, G. C., Lo, M. S., Reis, P. C. & Sullivan, K. E. New insights into the immunopathogenesis of systemic lupus erythematosus. *Nat. Rev. Rheumatol.* **12**, 716–730 (2016).
- Lee, J. C. & Smith, K. G. C. Prognosis in autoimmune and infectious disease: new insights from genetics. *Clin. Transl. Immunol.* **3**, e15 (2014).
- Stoeckius, M. et al. Simultaneous epitope and transcriptome measurement in single cells. *Nat. Methods* **14**, 865–868 (2017).
- Lu, Y. et al. Systematic analysis of cell-to-cell expression variation of T lymphocytes in a human cohort identifies aging and genetic associations. *Immunity* **45**, 1162–1175 (2016).
- Nakaya, H. I. et al. Systems analysis of immunity to influenza vaccination across multiple years and in diverse populations reveals shared molecular signatures. *Immunity* **43**, 1186–1198 (2015).
- Querec, T. D. et al. Systems biology approach predicts immunogenicity of the yellow fever vaccine in humans. *Nat. Immunol.* **10**, 116–125 (2009).
- Langfelder, P. & Horvath, S. WGCNA: an R package for weighted correlation network analysis. *BMC Bioinf.* **9**, 559 (2008).
- Li, S. et al. Molecular signatures of antibody responses derived from a systems biology study of five human vaccines. *Nat. Immunol.* **15**, 195–204 (2014).
- Muskardin, T. L. W. & Niewold, T. B. Type I interferon in rheumatic diseases. *Nat. Rev. Rheumatol.* **14**, 214–228 (2018).
- Butler, A., Hoffman, P., Smibert, P., Papalexi, E. & Satija, R. Integrating single-cell transcriptomic data across different conditions, technologies, and species. *Nat. Biotechnol.* **36**, 411–420 (2018).
- Swiecki, M. & Colonna, M. The multifaceted biology of plasmacytoid dendritic cells. *Nat. Rev. Immunol.* **15**, 471–485 (2015).
- Jego, G. et al. Plasmacytoid dendritic cells induce plasma cell differentiation through type I interferon and interleukin 6. *Immunity* **19**, 225–234 (2003).
- Gricks, C. S. et al. Differential regulation of gene expression following CD40 activation of leukemic compared to healthy B cells. *Blood* **104**, 4002–4009 (2004).
- Shimabukuro-Vornhagen, A. et al. Inhibition of protein geranylgeranylation specifically interferes with CD40-dependent B cell activation, resulting in a reduced capacity to induce T cell immunity. *J. Immunol.* **193**, 5294–5305 (2014).
- Elgueta, R. et al. Molecular mechanism and function of CD40/CD40L engagement in the immune system. *Immunol. Rev.* **229**, 152–172 (2009).
- Arriens, C., Wren, J. D., Munroe, M. E. & Mohan, C. Systemic lupus erythematosus biomarkers: the challenging quest. *Rheumatology* **56**, i32–i45 (2017).
- Verheul, M. K., Fearon, U., Trouw, L. A. & Veale, D. J. Biomarkers for rheumatoid and psoriatic arthritis. *Clin. Immunol.* **161**, 2–10 (2015).
- Banchereau, J. & Pascual, V. Type I interferon in systemic lupus erythematosus and other autoimmune diseases. *Immunity* **25**, 383–392 (2006).
- Quách, T. D. et al. Distinctions among circulating antibody-secreting cell populations, including B-1 cells, in human adult peripheral blood. *J. Immunol.* **196**, 1060–1069 (2016).
- Andrews, S. F. et al. High preexisting serological antibody levels correlate with diversification of the influenza vaccine response. *J. Virol.* **89**, 3308–3317 (2015).
- He, X.-S. et al. Baseline levels of influenza-specific CD4 memory T-cells affect T-cell responses to influenza vaccines. *PLoS One* **3**, e2574 (2008).
- Patin, E. et al. Natural variation in the parameters of innate immune cells is preferentially driven by genetic factors. *Nat. Immunol.* **19**, 302–314 (2018).
- Westra, H. J. et al. Systematic identification of trans eQTLs as putative drivers of known disease associations. *Nat. Genet.* **45**, 1238–1243 (2013).
- Klein, S. L. & Flanagan, K. L. Sex differences in immune responses. *Nat. Rev. Immunol.* **16**, 626–638 (2016).
- Rees, F., Doherty, M., Grainge, M. J., Lanyon, P. & Zhang, W. The worldwide incidence and prevalence of systemic lupus erythematosus: a systematic review of epidemiological studies. *Rheumatology* **56**, 1945–1961 (2017).
- Zyla, J. et al. Gene set enrichment for reproducible science: comparison of CERNO and eight other algorithms. *Bioinformatics* **35**, 5146–5154 (2019).
- Korotkevich, G., Sukhov, V. & Sergushichev, A. Fast gene set enrichment analysis. Preprint at bioRxiv <https://doi.org/10.1101/060012> (2019).

Publisher's note Springer Nature remains neutral with regard to jurisdictional claims in published maps and institutional affiliations.

© The Author(s), under exclusive licence to Springer Nature America, Inc. 2020

Methods

Datasets. A summary of the datasets used in our study can be found in Supplementary Table 2. See also the ‘Life Sciences Reporting Summary’ accompanying this paper and the Data Availability section.

Software. A summary of the software packages used and their versions can be found in Supplementary Table 8. See also the ‘Life Sciences Reporting Summary’ accompanying this paper and the Code Availability section.

Predictive B cell populations. PBMC sample collection and processing are described previously¹². The predictive baseline B cell populations identified¹² (ID103, ID96, ID91, ID108; Fig. 6 and Table S2 in ref. ¹²) had two important features: (1) high temporal stability (low within-subject variation (WSV) with high inter-subject variation (ISV) (Fig. 2 in ref. ¹²); and (2) a positive correlation between the baseline/pre-vaccination cell frequencies and vaccine antibody response as quantified by the adjusted maximum fold change (adjMFC) (Fig. 6C in ref. ¹²). The adjMFC is a measure of antibody fold-change following vaccination after removing the nonlinear correlation between the maximum (log) fold change in antibody response and the baseline antibody titre, thus allowing for evaluation of predictive factors that are independent of the baseline antibody titre (see Methods in ref. ¹²). As in ref. ¹², for all the influenza vaccination datasets we assessed in this study, we used the adjMFC metric to reflect the maximum titre to any of the vaccine components administered to a given subject, especially because the above B cell populations of interest, and therefore the associated transcriptional surrogate signatures we explored here, were not measured in an antigen-specific manner.

Flow cytometry data processing. See also the ‘Life Sciences Reporting Summary’ accompanying this paper. All flow cytometric quality control (for example, sample exclusion) and gating was performed before the analyses described below, for example, predictive modelling and surrogate transcriptional signature (TGSig) derivation. We gated four new subpopulations (based on CD38 and CD10 markers) inside the CD45⁺CD19⁺CD20⁺ live B cell gate (FlowJo ver.9.9.3 TreeStar/Becton Dickinson, Ashland, OR, on Mac OS X; Fig. 1b and Extended Data Fig. 1a). Gate 1: CD38⁺ cells with CD38 (G610-A; PE-Texas Red) fluorescent intensity greater than 1,000; gate 2: CD38⁺⁺ cells with fluorescent intensity greater than 10,000; gate 3: CD38⁺⁺CD10⁺ cells with CD10 (R780-A; APC Cy7) fluorescent intensity greater than 1,000; gate 4: CD38⁺⁺CD10⁻ cells with CD10 fluorescent intensity less than 1,000. We exported cell frequencies, expressed as the percentage of the parent population. The above gating strategy was designed based on the following considerations: (1) high CD38 expression was a common feature among the predictive CD20⁺ B cell populations from ref. ¹². (2) CD10-based gates were included because CD10 was expressed in one of the original predictive populations (ID91; Fig. 6 and Table S2 in ref. ¹²), and these gates would also allow us to evaluate prediction performance with or without the inclusion of CD10 gates (Fig. 1b and Extended Data Fig. 1a). Note that delineating CD10⁺ versus CD10⁻ cells in healthy individuals can be challenging⁴¹, so we were cautious in our interpretation of the CD10⁺/CD10⁻ fractions and focused solely on evaluating relative prediction performance with or without the inclusion of our CD10 gates in CD20⁺CD38⁺⁺ cells (Fig. 1b and Extended Data Fig. 1a).

Quality control. Based on visual evaluation during gating, specifically taking into account: (1) low cell viability (<70%); (2) the extremely small number of cells expressing high levels of CD38 (less than 5 cells in the CD38⁺⁺ gate); (3) non-discriminable B cell populations (visually indistinct CD19⁺ population in CD45⁺ cells), we excluded 8 baseline samples (out of 78 baseline samples that had titre data published in ref. ¹² and were either high or low responders based on adjMFC—only high/low responders were used in the subsequent analyses described below, although middle responders were also used to assess robustness (Extended Data Fig. 3); here, again, baseline was defined as days 0, -7 and 70. Note that subject 262 (all three baseline time points) was not used in subsequent analysis because they were at first erroneously labelled as an intermediate responder, but during final quality checks they were identified as a high responder. In general, we followed the above cutoffs to remove samples, except that we also removed the day 70 sample of subject 250 (viability 78.1% and 20 counts of CD38⁺⁺ cells) because the percent of CD38⁺⁺ cells was much lower than day 0 (0.63% versus 3.38%). After quality control, we have the following number of samples for subsequent analyses:

	Low responders	High responders
Baseline 1 (day 0)	11	12
Baseline 2 (day -7)	11	12
Baseline 3 (day 70)	10	11

Selection of CD19⁺CD20⁺CD38⁺⁺ population (CBSig). The predictive power of each of the four newly gated cell subsets (Fig. 1b and Extended Data Fig. 1a) were evaluated by AUC (see ‘Performance assessment of model predictions’). Of the four cell populations, population no. 2 (CD38⁺⁺ of CD20⁺ B cells) had the highest AUC (Fig. 1b) and was selected as the population of interest (CBSig, red box). Note that

the addition of CD10 in the gating scheme (CD10⁺CD38⁺⁺ versus CD10⁻CD38⁺⁺) led to lower AUCs compared to CBSig, but the CD10⁺ and the CD10⁻ subsets had similar predictive performance, indicating that CD10 status was not important for prediction (Fig. 1b). Variations of this gating scheme, such as lowering the CD38 expression level requirement or using CD10 to restrict to transitional or non-transitional subsets, did not result in better prediction performance (Fig. 1b), suggesting that CD19⁺CD20⁺CD38⁺⁺ cells were indeed a core predictive population.

Construction of a ten-gene signature (TGSig). Microarray data processing

To develop a gene-based surrogate predictive signature of CBSig, we used the same influenza vaccination dataset from our previous study (the NIH Center for Human Immunology (NIH/CHI) dataset) in which gene expression data was also generated from the same PBMC samples assessed by flow cytometry¹². The raw gene expression data are available in GEO (GSE47353); the processed data are available on our data portal (<https://chi.niaid.nih.gov>). The expression data was RMA-normalized and batch-corrected as described in the ‘Extended experimental procedures’ section (‘Low-level microarray data processing’ section) in ref. ¹². Briefly we found that the hybridization date (batch) of array was significantly correlated with most probe sets, and we removed this effect using linear regression for each probe set individually. For this purpose, for the i -th probe set we fitted the model (i -th probe set intensity) \sim (hybridization date), and only retained the residuals from this fit.

Assessing temporal stability. To derive a surrogate gene signature, we looked for genes that: (1) correlated with the frequency of CD20⁺CD38⁺⁺ B cells prior to vaccination (day 0); (2) have low within-subject variation across the three baseline time points (so that it is temporally stable); and (3) have high ISV to help potentially delineate differences in responsiveness.

Here we have a data vector $X = \{x_{ij}\}$ (individual, i ; time point, j), where each x_{ij} is associated with a subject and each subject has three measurements obtained from each of the baseline time points. We then fitted a one-way ANOVA model (in R notation: $X \sim \text{subject}$) to evaluate the total variance (total sum of squares) and partitioned the total sum of squares into components attributable to subject-to-subject variation and the rest as the fitted residual.

$$SS_{\text{total}} = SS_{\text{subject}} + SS_{\text{residual}}$$

SS_{subject} is the sum of squares of differences between the subject mean and the overall mean. SS_{residual} is the remaining sum of squares. Here we assumed that the variance explained by SS_{subject} provides an estimate of subject-to-subject differences whereas the variance explained by the residual of this fit (SS_{residual}) provides an estimate of the sum of within-subject variation and other sources of noise, including technical noise. We then used this relationship:

$$1 = \frac{SS_{\text{subject}}}{SS_{\text{total}}} + \frac{SS_{\text{residual}}}{SS_{\text{total}}}$$

to evaluate the fraction of variance explained by subject ($SS_{\text{subject}}/SS_{\text{total}}$; ISV) relative to the fraction explained by the residual of the fit ($SS_{\text{residual}}/SS_{\text{total}}$). We defined ($SS_{\text{subject}}/SS_{\text{total}}$; ISV) as the ‘stability score’, or the temporal stability metric (TSM), insofar as high ISV would indicate low residual variance and thus higher temporal stability within subjects over time. Quality controlled expression data from all three baseline time points were used in this analysis (see workflow below and ref. ¹² for quality control procedures.)

Selection and evaluation of signature genes. We selected a total of 726 genes with TSM ≥ 0.75 for correlation analysis. Using only data from the high and low responders with both day 0 flow cytometry (see above) and gene expression data passing quality control in the NIH/CHI dataset (22 day 0 samples in total), we correlated these 726 genes against the frequency of CD20⁺CD38⁺⁺ cells using day 0 data. To mitigate influence from outlier subjects and account for sampling noise, we used multiple iterations of subsampling of the cohort to derive a ‘robust’ measure of correlation as follows: in each iteration, we excluded two subjects and then calculated the Spearman correlation between each gene and the cell frequency. We performed a total of 231 iterations (the number of subject combinations to exclude 2 out of the 22 subjects). For each gene, the ‘robust correlation’ is defined as the average correlation divided by its standard deviation across all iterations. Genes were ranked according to this robust correlation statistic, which considers both the magnitude of the correlation and sampling noise. Top genes from the list can be found in Supplementary Table 1 together with additional information, including the mean, standard deviation and the percent of iterations in which the gene was ranked among the top 20.

To determine the number of top genes to construct the surrogate signature, we compared AUCs generated from top k genes ($k = 1, 2, 3, \dots, 30$) (see ‘Gene-based signature score calculation’) for the three baseline time points (Extended Data Fig. 2c). We empirically chose k ($k = 10$, TGSig) so that the AUC was maximized in all three time points while including a sufficient number of genes so that when we evaluate the signature in other datasets with different profiling platforms we can retain a reasonable number of these genes. In addition, we checked how exclusion

of any single gene from the signatures affects prediction performance (Extended Data Fig. 2g).

To estimate the null distribution of prediction performance, we generated a set of 500 ‘random signatures’—top 10 genes based on the same ranking and evaluation scheme described above, except that the gene–cell population correlations were calculated using subject-label permuted data without applying the temporal stability filters. We used these ‘random signatures’ generated for each dataset to evaluate whether the prediction performance of our signature is significantly higher than that expected by chance (Extended Data Fig. 2e).

Finally, we also checked that our signature genes retained their relative rank even if we relaxed the stability (TSM) threshold. Because the total number of ‘temporally stable’ genes is dependent on the stability threshold, instead of using absolute ranks we normalized the ranks of signature genes by the total number of genes passing the stability threshold (Extended Data Fig. 2f). The ranking of the top genes is relatively stable across TSM thresholds of ≥ 0.75 , although additional random noise dominates when the TSM threshold exceeds 0.75 because the number of genes became small (Extended Data Fig. 2f).

Gene set-based signature score calculation. Given a set of signature genes (for example, TGSig) and a dataset (for example, Yale 2011), we calculated the signature scores for each dataset independently. Due to profiling platform differences, some genes in a signature were not present in a given dataset and those genes were not used in the signature score computation. We used a z score transformation to standardize the expression of each gene to have mean 0 and standard deviation 1 across all the samples in the dataset. This step was carried out to ensure that expression values of different genes were on the same scale and thus comparable. The signature score of a sample was then calculated by averaging the standardized expression value of the signature genes (Extended Data Fig. 2d).

Evaluation of TGSig in non-CHI vaccination datasets. Dataset selection and data preparation. We obtained influenza vaccination datasets from a recent meta-analysis of transcriptomic signatures of influenza vaccination conducted by the Human Immunology Project Consortium and CHI¹⁰. These data were derived from PBMC (SDY400 and SDY404) or whole blood (SDY212) (Supplementary Table 2). We downloaded the pre-processed expression data from ImmuneSpace (<http://immunespace.org>) using the ImmuneSpaceR Bioconductor package⁴². These studies are also available on ImmPort (<http://immpore.org>) under study IDs SDY212 (Stanford University, season 2008–2009), SDY400 (Yale University, season 2012–2013) and SDY404 (Yale University, season 2011–2012). See also the ‘Life Sciences Reporting Summary’ accompanying this paper.

The influenza vaccination dataset previously published¹⁸ (Emory; seasons 2008–2011) was downloaded from GEO ([GSE29619](https://www.ncbi.nlm.nih.gov/geo/query/acc.cgi?acc=GSE29619) and [GSE74817](https://www.ncbi.nlm.nih.gov/geo/query/acc.cgi?acc=GSE74817)). The demographics and HAI titre data were received via private communication. Season 2007 was excluded from the analysis due to the small number ($n=9$) of subjects. The downloaded data (matrix data (probeset \times sample) from GEO) was already pre-processed (including normalization and log-transformation), and we thus used it unaltered in our analysis. We also conducted the same analyses by starting from the raw CEL files (using the same procedure as described below for yellow fever) and the results were similar to Extended Data Fig. 3c (data not shown.) We also tested defining high and low responders using the same method as reported in the original publication¹⁸ and the results were again similar in that the high and low responders were not separable statistically (data not shown).

The yellow fever vaccination dataset¹⁹ was downloaded from GEO ([GSE13486](https://www.ncbi.nlm.nih.gov/geo/query/acc.cgi?acc=GSE13486)). Since the pre-processed data was not available, we downloaded the CEL files and performed background correction and normalization of the expression data with RMA algorithm implemented in Affymetrix Power Tools (APT) version 1.18.1 (ThermoFisher).

The systemic lupus erythematosus (SLE) dataset¹³ was downloaded from the webSLE data portal (<http://websle.com>) as an RData file, which contained ExpressionSet objects with pre-processed and pre-filtered expression data together with probe annotation and sample information.

For expression datasets containing only probe level information, we summarized probe level expression into gene level data as follows: (1) we retained only probes that were unambiguously mapped to a single gene; (2) in the case where multiple probes were mapped to the same gene, we performed principal component analysis of the probes using all samples in the dataset, and then selected the probe maximally correlated with the first principal component as the reporter for the expression of the gene.

All expression data were RMA normalized and log2-transformed before analysis, except for the SLE data where we used the pre-processed data directly (which included log2-transformation.)

Note that for the NIH/CHI dataset, TGSig was computed only for subjects with both quality controlled gene expression and titre data (see workflow below.)

Identification of high and low responders. High and low responder determination was performed before and independent of any predictive signature assessment. We used the adjMFC metric to quantify the antibody response to influenza vaccination independent of the initial/baseline titre^{2,10}). While there were differences in how antibody titre data were generated across different datasets/studies (for example, the NIH/CHI dataset used microneutralization assays, while others used the

haemagglutination inhibition (HAI) assay), adjMFC only reflects the normalized, relative response within a dataset/cohort, but not the absolute magnitude (see ref. ¹²) and is thus applicable to all datasets to quantify the relative response (high versus low responders) within each dataset. The detailed methodology can be found in the ‘Extended Experimental Procedures’ and ‘Titre definitions’ sections in ref. ¹².

For each of the influenza vaccination datasets, we classified subjects into high and low responders according to their adjMFC values, and use these response class labels in subsequent analyses (see refs. ^{12,10} for the rationale behind focusing only on high and low responders). Briefly, subjects who were below the 30th percentile or above the 70th percentile adjMFC values in a dataset were classified as low and high responders, respectively. Following previous HIPC-CHI analyses, these thresholds were selected to allow enough high and low responders for analysis. This cutoff differs from that used in the original NIH/CHI influenza study, in which the subjects were discretized to low and high responders using the 20th and 80th percentile adjMFC values as cutoffs, respectively (see Methods in ref. ¹²). To be consistent with the original NIH/CHI influenza study, we kept the same 20/80 cutoffs for defining high and low responders when analyzing the NIH/CHI dataset here. These cutoffs were all pre-determined before analyses started.

For the yellow fever vaccination dataset, neutralization titres against the yellow fever virus (YFV) measured on day 60 were used as the antibody response to vaccination because all subjects were naive to the YFV at baseline. We discretized the original titre values within each of two reported trials. The thresholds to identify high and low responders were selected based on the distribution of titre values within each trial. Because the neutralizing titres were measured using different techniques (by cytopathic effect (CPE) for trial 1 and by plaque reduction neutralization test (PRNT) for trial 2), the exact thresholds we used were different. For trial one, six subjects were classified as low responders (titre < 160), and six as high responders (titre > 160), while for trial two there were three low responders (titre < 640) and four high responders (titre > 640). Titre values of 160 and 640 were considered ‘middle responders’ in each trial, respectively, and were excluded from analysis.

Predictive performance assessment. To assess whether TGSig was predictive of high versus low responders, we computed the AUC (area under the empirical receiver operating characteristic (ROC) curve). A permutation procedure was used for estimating one-tailed P values—see below for further details. We also used the one-tailed Wilcoxon Rank Sum test to assess whether the signature score was significantly higher in high compared to low responders, which also provided another measure of statistical significance in addition to that computed for the AUC. We used a one-tailed test because we knew a priori that CBSig (and the original predictive populations from ref. ¹² from which TGSig was derived) had higher frequencies in high than in low responders. Thus, we specifically test whether TGSig (a surrogate of CBSig) was significantly higher in high than low responders. All statistical analyses were performed using R/Bioconductor. ROC curves were computed with the ‘pROC’ package⁴⁴.

Assessing TGSig in independent vaccination datasets. After selecting signature genes for TGSig using only the day 0 data of the CHI influenza dataset, we computed the TGSig signature scores for each subject prior to vaccination in each of the influenza vaccination datasets (Stanford, Yale and Emory) and the yellow fever vaccination dataset, and evaluated the predictive performance of delineating high versus low responders. The influenza datasets all had bi-modal age distributions (young, age < 35 years; older, age > 60 years) because they were originally designed to assess responses in older versus younger individuals¹⁰; we thus focused on testing TGSig in young subjects only because the CHI dataset consisted of largely younger individuals. We did evaluate TGSig in older subjects and found that it was not predictive of high versus low responders in those older than 60. For the Emory dataset, a higher cutoff for ‘young’ (age < 60 years) was employed because using a cutoff of 35 would result in a very small dataset, but we also tested using 35 as the cutoff and the results were similar. The yellow fever dataset contains two trials with the first having a larger sample size than the second, and we tested the signature in each trial independently.

Additional statistics for assessing prediction of high versus low responders can be found in Supplementary Table 2b.

Application of TGSig to a paediatric SLE cohort. See also the ‘Life Sciences Reporting Summary’ accompanying this paper. In the SLE study, each patient had multiple samples (visits) collected over time, each of which may be collected when the patient had different levels of disease activity as reflected by the SLEDAI score. The original publication¹³ defined seven groups of patients based on SLEDAI-associated gene expression patterns (correlation computed over time/multiple visits), and showed that for patient groups 2, 3 and 4, the SLEDAI score was correlated with genes associated with a plasma cell/plasmablast signature.

For reasons discussed in the main text, we focused on patients from groups 2, 3 and 4 and evaluated whether TGSig evaluated at low disease activity time points was correlated with the changes in plasmablast signature score associated with disease activity (for example, the extent of plasmablast score increase between low and high disease activity time points). Note that we used a mixed effect model to estimate this latter quantity (see below for details). For each patient in groups 2,

3 and 4, we calculated a plasmablast signature score for each visit (using the gene module DC.M4.11 as described below in ‘Plasmablast gene signature’). Because each patient had multiple visits and patients often had treatment (for example, corticosteroids) that, in turn, may have an effect on the changes in plasmablast score as a function of disease activity, we used a linear mixed effect model to integrate the data⁴⁵ (in R/lme4 notation): $PB \sim \sum T_i + SLEDAI | SUBJECT$, where PB is the signature score, T_i is an indicator of treatment group (as defined in the original paper), SLEDAI is treated as a continuous variable, and subject is treated as the random effect. Here the subject-dependent, ‘random’ coefficient for the SLEDAI term (the ‘slope’) would give us an estimate on the quantitative extent by which the plasmablast signature score would change as disease activity varies. Note that the plasmablast signature score is presumably reflective of plasmablast frequencies, as shown previously¹². We fitted the mixed effect model and extracted the aforementioned personal ‘slope’ by using the ‘ranef’ function; hereon we will refer to this patient-specific quantity as the ‘disease activity-associated change in plasmablasts (DaCP)’. We also tested treating SLEDAI as a discrete/categorical variable (high and low disease activity only, or high, middle and low disease activity—see below for definition) and the resulting estimate for the personal DaCP was similar to that obtained by treating SLEDAI as a continuous variable (data not shown). We further assessed the robustness of DaCP by comparing it to the simple difference between the average plasmablast score of high disease activity time points and that of low disease activity time points (Extended Data Fig. 5b), and as expected they were highly correlated.

To compute TGSig from clinically quiescent or ‘baseline’ low disease activity time points, we adopted the original SLE study’s classification of samples into low, middle and high disease activity groups based on the SLEDAI score (low, SLEDAI < 3; medium, SLEDAI = 3–7; high, SLEDAI ≥ 8). We then calculated the TGSig score at low disease activity time points. Because each subject may have more than one sample from a low disease activity time point, subject-specific scores were computed by averaging the score from all low disease activity time points. We then tested whether the TGSig signature score calculated at low disease activity time points was correlated with DaCP. As a control, we performed the same analysis described above in patient groups 1, 5, 6 and 7 to assess if such a correlation exists for patients whose disease activity did not correlate with plasmablast scores.

Plasmablast gene signature. We chose the gene set DC.M4.11 ‘Plasma cells’ from the Chauhan BTMs to compute the plasmablast signature score⁴⁶ because: (1) this was one of the plasma cell/plasmablast gene signatures that the original SLE study found to be correlated with disease activity (that is, which helped define patient groups 2, 3 and 4); (2) we examined the within-module gene–gene correlation in this and additional plasmablast related gene modules (see below) and found that this gene set had the best coherency and exhibited the highest overall gene–gene correlations; and (3) the score of DC.M4.11 was significantly correlated with the score computed from a gene set we derived earlier based on correlation with changes in plasmablast frequency on day 7 following influenza vaccination (see Fig. 7B in ref.¹²) (data not shown), thus suggesting that the signature score computed from DC.M4.11 was directly reflective of plasmablast frequencies.

From ref. ⁴⁶

DC.M4.11	Plasma cells
DC.M7.7	Undetermined
DC.M7.32	Undetermined
From ref. ²¹	
LI.M156.0	Plasma cells and B cells, immunoglobulins
LI.M156.1	Plasma cells, immunoglobulins

Computing gene set enrichment scores for transcriptional differences between high and low disease activity periods. For each gene and patient, we first computed the average gene expression for samples with high disease activity (or middle disease activity if no samples with high disease activity were available) and separately for those with low disease activity. Then for each subject the genes were ranked by the magnitude of the difference between these two average values (high disease activity—low disease activity), followed by gene set enrichment analysis using the CERNO test from the ‘tmod’⁴⁷ R package to generate the enrichment statistics for each subject and gene set. The enrichment for each gene set in each subject is shown as $-\log_{10}$ of the FDR-adjusted P-value in the heatmap of Extended Data Fig. 5a. To summarize the information in this heatmap and show patient group dependent enrichment, we averaged the enrichment values across each patient group and gene sets with similar phenotypic annotations (as determined previously in the original publication¹²) and generated the compressed heatmap of Fig. 2c.

Identification and characterization of co-expression modules at low disease activity time points. To identify co-expression modules in SLE patients, we first calculated the average expression profile for each patient using samples from low disease activity time points. We focused also on temporally stable genes (across

low disease activity time points) because those are more likely to reflect stable, personal immune states. We estimated the TSM score for each gene across low disease activity time points using a similar approach as described above for the development of TGSig in the NIH/CHI influenza dataset, except that stable genes were selected using a more relaxed cutoff, that is, using a FDR cutoff of 0.05 (calculated from the P values of the F statistics of the ANOVA model above), which resulted in 9,601 ‘stable’ genes, because we wanted to retain more genes for module analysis. We next used the WGCNA algorithm to determine modules²⁰. We determined the algorithm’s hyperparameters following the authors’ recommended procedure, setting soft power to 4 (the lowest power for which the scale-free topology fit index curve flattens out upon reaching a high value; in this case, roughly 0.80), and network type to ‘signed hybrid’. We were able to assign ~2,800 genes to 18 co-expression modules (Supplementary Table 3), with module size ranging from 25 to 719 genes (Fig. 3a and Supplementary Fig. 1a).

To assess the extent by which these modules were associated with the DaCP, we calculated the Pearson correlation between the eigengenes of each module (that is, PC1) and the DaCP. To evaluate statistical significance, we generated an empirical null distribution for each module by randomly shuffling subject labels and recalculating correlations on the shuffled data (Supplementary Fig. 1b). Empirical P values were determined by comparing the actual correlations with the corresponding null distributions.

For functional characterization, we evaluated whether the modules are enriched for known gene sets (such as the BTMs²¹, Supplementary Fig. 1c) with the hypergeometric test. The false discovery rate was controlled using the Benjamini–Hochberg procedure⁴⁸.

Meta-analysis to identify genes associated with vaccine responses. We used random effect meta-analysis models⁴⁹ to estimate the ‘meta’ effect size of each gene by combining expression and antibody response data from multiple vaccination datasets. This method models the observed effect size y_i (association between expression and vaccine response class as reflected by adjMFC high versus low responders for each study i) as a draw from a distribution with study-specific mean θ_i and variance s_i^2 (that is, intra-study sampling error). Furthermore, each θ_i is assumed to be a draw from a distribution with overall mean μ and variance τ^2 (that is, inter-study variability):

$$y_i = \theta_i + \epsilon_i, \quad \epsilon_i \sim N(0, s_i^2)$$

$$\theta_i = \mu + \delta_i, \quad \delta_i \sim N(0, \tau^2)$$

We identified influenza response genes by applying the method to the four influenza vaccination studies (Supplementary Table 4a). We only evaluated the temporally stable genes as defined above based on the low disease activity time points because those were the genes we used to define co-expression modules. In addition, we applied the same method to the two trials of yellow fever vaccine. We found that the meta-analysis results are largely consistent with the first trial, but much less so with the second trial (data not shown). The relatively poor coherence between the two trials may be partly due to the very small sample size of the second trial (only 7 subjects). Our observation suggested that inclusion of data from trial two is more likely to introduce noise than signal, thus we decided to only focus on trial one.

Gene set enrichment analysis. Gene set enrichment analysis (GSEA) is a widely used approach to test if a particular gene set is enriched at the top of a ranked gene list⁵⁰. Because the datasets we used are from peripheral blood samples, we decided to use known gene sets from the same tissue: the BTMs²¹. These gene modules were identified from network analysis of gene–gene correlations in multiple blood transcriptomic datasets. We used an efficient implementation of GSEA analysis from the ‘fgsea’ R package⁴⁰ with the BTM modules from the ‘tmod’ R package⁴⁷ (‘fgsea’ was used also to extract leading edge genes.)

We applied GSEA to assess whether the genes in the ‘brown’ co-expression module identified in the SLE cohort are enriched at the top of the genes ranked by their meta-effect/association with antibody response to influenza vaccination (Fig. 3d); we also performed the same analysis for yellow fever trial one (see above) but the result was statistically insignificant.

To test for enrichment of BTMs in genes from the NIH/CHI influenza dataset ranked by correlation with CD20⁺CD38⁺⁺ B cell frequency, we selected temporally stable genes with TSM ≥ 0.5 from the NIH/CHI influenza study dataset, and ranked them by their robust correlation metric (see ‘Baseline gene-based predictive signature’ above). Here a more relaxed temporal stability cutoff was used to increase the number of genes and statistical power for enrichment analysis. P values from the enrichment test were corrected for multiple-testing using the Benjamini–Hochberg method⁴⁸.

GSEA was also applied to identify ‘leading edge’ genes, a subset of the query set that maximizes the enrichment score. Applying leading edge analysis to brown module and the genes from the NIH influenza study ranked by correlation with CD20⁺CD38⁺⁺ B cell frequency, we identified a set (87 genes) of leading edge genes in the brown module (and called this gene set SLE-Sig) (Fig. 3e and Supplementary Table 5). To better understand the predictive property of genes in the brown

module, we divided it into two subsets—the leading-edge set (87 genes—SLE-Sig), and the remaining genes. For each subset, we calculated the eigengene and used it in regression analysis (Extended Data Fig. 6).

Assessing the relative contribution of TGSig and SLE-Sig to predicting vaccination responses. We used logistic regression to model association with vaccine response (high vs. low responder based on adjMFC) by pooling all four influenza vaccination datasets (Extended Data Fig. 6). We fitted three models, all having the following form (high responder: response = 1; low responder: response = 0):

$$Pr(response = 1) = X \cdot \beta + \epsilon$$

where X is a matrix of covariates, and β is a vector of coefficients estimated from the data. Model 1 includes both TGSig and SLE-Sig (represented by the eigengene or PC1 of genes in the respective set) as covariates, while models 2 and 3 only include one of the two covariates. In addition, all three models include dataset ID (encoded by dummy variables) as a covariate. To assess statistical significance, we performed the likelihood ratio test comparing two nested models (for example, model 1 and model 2).

The same approach was used to evaluate the relative contribution of TGSig and: (1) genes outside the leading edge in brown module; (2) IFN-I-DCact genes. Similarly, instead of evaluating vaccine responses, we applied this same approach to evaluate the relative contribution of TGSig and these other gene signatures in predicting DaCP in SLE.

Sorting of B cell populations from healthy donors. Peripheral blood mononuclear cells (PBMCs) were obtained from peripheral blood of six healthy individuals by density-gradient centrifugation and cryopreserved until day of B cell analysis and sorting. Multicolor flow cytometry was performed to identify PBMC B cell populations (Extended Data Fig. 7a) using the following mAbs: CD19-PerCP-Cy5.5, CD27-PE-Cy7 (ThermoFisher); CD20-APC-H7, CD38-BV421 (BD Biosciences); CD3-BV510 (Biologend). For transcriptional analysis, total CD19⁺CD20⁺ and CD19⁺CD20⁺CD38^{hi} B cells (5,000 each) were sorted into Trizol LS (Sigma) or ATACseq buffer using a FACSaria II (BD Biosciences). Flow data analyses were performed using FlowJo software (TreeStar/Becton Dickinson, Ashland, OR). Purity of B cell sorts was ~99%.

Donor demographic information is available in Supplementary Table 9. See also the ‘Life Sciences Reporting Summary’. Healthy donors were recruited under NIH IRB approved protocol NCT00001281. Informed consent was obtained from all study participants.

RNA-seq library preparation and analysis. RNA was isolated from cells sorted into Trizol LS using the Zymo Direct-zol Micro-prep columns (Zymo Research, Irvine, California). Total RNA sequencing libraries were prepared using the NuGEN SoLo RNA-seq library kit (NuGEN Technologies, San Carlos, California) according to the manufacturer’s instructions, using 1 ng of RNA as input. Libraries were sequenced using the Illumina NextSeq with version 2 sequencing reagents to an average of 20 million paired-end 37 base pair length reads per sample. Fastq files were generated from raw sequencing data using ‘bcl2fastq’ version 2.17.1.14 (Illumina). Reads were mapped using STAR³¹ version 2.5.2 aligner and the UCSC hg19 genome annotation and the —quantMode GeneCounts option. Counts-per-feature data output from STAR was imported into R 3.4.1. The average number of exonic-feature mapped counts was 3.14 million per sample. Differential gene expression was estimated using the ‘DESeq2’ package³². Mplot shown in Extended Data Fig. 7b was produced using ‘ggplot2’³³ version 2.2.1 (<https://cran.r-project.org/web/packages/ggplot2/index.html>).

Statistical evaluations. All statistical analyses were performed in R version 3.4.1, except for the low-level processing of single-cell data and some of the analyses in CITE-seq and RNA-seq (for example, Extended Data Figs. 7–9), which were performed using R 3.6.1. Effect sizes and *P* values of Pearson and Spearman correlations were computed using the ‘cor.test’ function. *P* values for Wilcoxon Rank Sum Test were computed using the ‘wilcox.test’ function. Unless noted, all Wilcoxon tests were two-tailed. Hedges’ *g* effect sizes were computed using the ‘cohen.d’ function in the ‘effsize’³⁴ package. Meta-analysis was performed with the ‘MetaDE’³⁵ package. Enrichment analysis was performed using the ‘fgsea’³⁰ package in Bioconductor (when we want to extract leading edge genes; the similar CERNO test was used when leading edge genes are not needed, for example, Fig. 2c and Extended Data Fig. 5a) Jonckheere-Terpstra trend test for ordered differences among multiple classes was performed using the ‘jonckheere.test’ function in the ‘clinfun’ package³⁶. Area under ROC curve (AUC) and 95% confidential interval were computed using the ‘pROC’ package⁴⁴. The *P* value for AUCs was estimated by a permutation procedure: we shuffled the subject labels to create a mismatch between the responder class and the gene expression data and generated 1,000 permutations test the null hypothesis that the observed AUC was drawn from this null distribution. Metrics to further assess prediction performance (Supplementary Table 2b) were computed using the ‘MLmetrics’ package³⁷. Some metrics required a cutoff for calling high vs. low responders: (1) for gene expression based predictors we used zero since we used scaled (z-score based) gene expression values to

compute the score of a gene set for each subject; (2) for cell frequency based predictors the cutoff was set to the median of cell frequencies.

Simultaneous protein and transcriptomic single cell profiling via CITE-seq.

Combined surface target protein and mRNA expression single cell analysis was performed using the CITE-seq methodology according to refs. ^{16,58,59} with the following modifications: $n=20$ high and low responders were split between two experimental batches with $n=5$ high and $n=5$ low responders in each batch. See also the ‘Life Sciences Reporting Summary’. The high and low responder groups were not significantly different in age and sex ($P=0.16$ for age and $P=0.37$ for sex, Wilcoxon two-tailed test). In each batch, samples were stained using cell ‘hashing’⁵⁸ antibodies such that samples could be demultiplexed using a combination cell hashing identifiers and SNP genotype demultiplexing⁶⁰. After cell hashing antibody staining, cells from each batch were pooled into one tube and stained with a mixture of oligo-labelled antibodies against target surface proteins. The two experimental batches were performed on consecutive days, using aliquots of the same pool of antibodies for each batch. Final antibody concentrations used for staining were determined using titration experiments; the concentration of antibody that appeared to saturate ligand was utilized, or for cases in which apparent saturation was not reached, the manufacturer’s recommended amount was used. Oligo-labelled antibodies for cell hashing and surface target protein detection were obtained from Biologend (see Supplementary Table 10 for list of reagents). The same pool of donor cells from each batch were distributed evenly across 6 lanes of 10x Genomics Single Cell 3’ expression reagents (version 2). Cell hashing (HTO) and surface target protein (ADT) libraries were prepared according to^{16,58,59}. cDNA tag libraries were prepared using the 10x Genomics v2 kit according to manufacturer’s instructions. Libraries were sequenced using the Illumina HiSeq 2500 and v4 reagents. Additional statistics: mean number of gene detected per cell was 746, mean number of unique molecular identifiers (UMI) per cell was 2139. The mean read depth per cell was approximately 43,000–84,000 as reported by CellRanger. The fraction of reads mapped to the genome was above 90% for all lanes; sequencing saturation was typically around 90%.

Computational low-level processing of CITE-seq data. *Bcl2fastq* version 2.20 (Illumina) was used to demultiplex the sequencing data. *CellRanger* version 3.0.1 (10x Genomics) was used for alignment (using the Hg19 annotation file provided by 10x Genomics) and counting UMIs. CITE-seq ADT and HTO tag alignment and UMI counting was done with CITE-seqCount⁶¹ version 1.4.2. The following computational analysis of CITE-seq data was performed using the *Seurat* 2.3.4 R package³³ and the *SingleCellExperiment* Bioconductor class⁶². Hashing antibodies were used to identify the response class (high vs. low adjMFC) in each batch. Samples demultiplexed with Seurat’s HTODemux k-means function corresponded to either one or two possible sample identities. Sample labels were then assigned to each cell using *demuxlet*⁶³; only cells that met the following conditions were retained: 1) the cell must be defined as a ‘singlet’ by both hash demultiplexing and *demuxlet*; 2) the identified donor from *demuxlet* must match either of the two expected donors based on HTO hashing.

Surface protein data normalization and denoising. We used DSB (Denoised and Scaled by Background), a method we developed for CITE-seq protein data denoising and normalization⁶³. Briefly, for each protein, ADT data was normalized by taking the log+1 of raw counts, then subtracting the mean and divided by the standard deviation of the corresponding antibody count from the same batch measured in negative droplets. In addition, to account for droplet-to-droplet differences in the ADT capture rate as well as background noise from unbound antibody, we denoised each cell by removing a covariate corresponding to the background counts for each cell using the *removeBatchEffect* function in *limma*⁶⁴ package; this covariate was defined for each cell as the eigenvector of: 1) the mean of non-staining antibodies in that cell; 2) counts from 4 isotype control antibodies. mRNA data was normalized with *scran*⁶⁵ after removing cells with greater or less than 3 median absolute deviations from the median library size.

Cell clustering and annotation. The cell clusters were identified by a shared nearest neighbour (SNN) modularity optimization based clustering algorithm⁶⁶ implemented in the ‘Seurat’ R package²³. Only ADT data (surface protein expression) were used to generate the Euclidean distance matrix computed for all single cells. The matrix was then used to build the SNN graph followed by *k*-nearest neighbours clustering ($k=50$). Three clustering resolutions were applied, 0.1, 0.3 and 1, to generate three sets of cell clusters; the relationship between these cluster sets were visualized using the ‘clustree’⁶⁷ and ‘ggraph’⁶⁸ R packages (Fig. 4b). The clusters were labelled accordingly to reflect this hierarchical relationship (for example C1 → C1.0 → C1.0.0). We annotated the protein-based clusters post hoc, linking them to canonical immune cell populations by visualizing both the average and distribution of all proteins in each cluster at multiple resolutions (Fig. 4c).

Single cell tSNE visualization. tSNE (t-distributed stochastic neighbour embedding) analysis was performed using ADT (surface protein expression) data only with the ‘RunTSNE’ function from the ‘Seurat’ package. Note that tSNE was used only for visualization. We used PCA for dimensionality reduction: the number of dimensions (7) used for tSNE was determined with the ‘elbow’ plot (not shown).

In the tSNE plot (Fig. 4a), the 10 clusters resulted from the resolution = 0.1 clustering above (with the perplexity parameter equal to 130) were shown.

Manual gating of CITE-seq data. To determine frequency of the CD19⁺CD20⁺CD38⁺⁺ B cell population for each subject, we first gated the total B cells in the dataset as CD3⁻CD56⁻CD14⁻CD19⁺. The gates were determined based on the density plot of each marker. We then applied the CD20⁺CD38⁺⁺ gate to total B cells. After we determined the cells in the gate, we used subject labels to compute the number of total B cells and CD20⁺CD38⁺⁺ B cells for each subject, and then the frequency of CD20⁺CD38⁺⁺ B cells as a fraction of the total number of cells.

Computing and evaluating subject-level gene set signature scores for cell clusters using CITE-seq data. Our goal was to assess, using only cells in a given cell cluster, whether the average (across single cells) relative expression of genes in a signature gene set is higher in the high responders compared to low responders. The procedure we devised below was used in two related situations: (1) given a bulk predictive signature (for example, TGSig), determine whether average relative expression of genes in the signature is significantly higher within a specific cluster of cells in high than low responders—this was used to uncover the cellular contributors to a bulk predictive signature such as TGSig; and (2) given a gene signature that reflects a cell state (for example, CD40act), assess whether a particular cluster of cells tends to have higher average relative expression of genes in the signature in high than low responders—when interpreting results from this analysis we are often making the assumption that higher average relative expression corresponds to a greater strength of signal that drove the cells to or kept the cells in that state. Thus, for the latter situation, we focused on signatures containing genes with evidence of increased expression when exposed to the ‘signal’ (for example, see CD40act below.) This assumption is sound because here we focus on genes that respond to signals such as CD40L and type I IFN, which lead to activation of transcriptional programs that shape the mRNA profile within specific types of cells.

There were two levels of averaging in our procedure: (1) averaging across single cells—single cell mRNA expression data can be noisy and since our goal here is to evaluate cell clusters, we took advantage of the power of statistical averaging to increase robustness and derive conclusions at the cell cluster level; (2) averaging across genes—information obtained from individual genes can also be noisy and often does not reflect cell states, which are typically more robustly captured by the level of multiple genes as a set of genes, for example, can be shaped by common upstream regulators. As also demonstrated by the success of methods such as GSEA and eigengene analysis, gene set level information can be more robust and can better reflect cell state shifts that affect multiple genes. Our single cell normalization procedure (see above) and simple z-score scaling (see below and ‘Gene set-based signature score calculation’ section above) helped to enable such averaging.

To compute the subject-level signature score for a gene set in a given cell cluster, we first created a cell-averaged gene expression data set for the cell cluster: for a given cell cluster and subject, we averaged the normalized single cell expression counts for each gene across single cells in that cell cluster for the subject. For each cell cluster (for example, cluster C0, naive CD4⁺ T cells; see Fig. 4b,c), this procedure generated a gene-by-subject expression matrix. We then applied the same z-score based procedure as we used for microarray gene expression data (see ‘Gene set-based signature score calculation’ section above) to compute the gene set signature score for each subject. We then used the non-parametric one-tailed Wilcoxon test to evaluate whether the signature scores are significantly higher in the high responders compared to the low responders.

As a robustness check for results involving the SLE-Sig signature (Fig. 5b), which is enriched for type I IFN responses and related processes (Fig. 3c,f), we also created another type I IFN gene signature (IFN, see Supplementary Table 6) using modules from an independent collection⁴⁶. This signature was created by combining (that is, the union) genes from the following three BTMs⁴⁶: DC.M1.2, DC.M3.4 and DC.M5.12.

Gene signature for CD40 activated B cells (CD40act). Our goal was to construct a transcriptional signature that reflects CD40 activation in human B cells. We focused on genes with evidence of increased expression following CD40L stimulation because we wanted to evaluate whether these genes tended to be elevated in B cells in high responders compared to low responders using CITE-seq data. The CD40act gene signatures (49 genes) was generated as the intersection between two gene sets (Supplementary Table 6). The first gene set (163 genes) was obtained by reading off the heatmap in Supplementary Fig. 1 in ref.²⁶, which corresponded to genes/probe sets with higher expression in CD40 activated B cells in comparison to mock-activated B cells (that is, those that appeared red and blue on the right and blue sides of the heatmap, respectively). Since the expression data was not available, we transcribed the probe set labels directly from the figure. The labels were then converted to probe set IDs with Affymetrix annotation and then converted to gene symbols by using the hgu95av2.db Bioconductor package⁶⁹. The second gene set (295 genes) were generated by using publicly available expression data from ref.²⁷. We downloaded the data from GEO (GSE54017) and selected genes more highly expressed in CD40 activated B cells than in resting B cells. The statistical cutoff was determined

using a one-sided paired *t*-test: we selected genes with an FDR-adjusted *P* value lower than 0.05 and a log2-fold-change greater than 1.5.

Reporting Summary. Further information on research design is available in the Nature Research Reporting Summary linked to this article.

Data availability

All data used in this study, including CITE-seq and flow data, are available at figshare (<https://doi.org/10.35092/yhjc.c.4753772>). The original/raw public gene expression data are available in the National Center for Biotechnology Information Gene Expression Omnibus (GEO) under accession numbers: GSE47353, GSE41080, GSE59654, GSE59743, GSE29619, GSE74817, GSE13486 and GSE65391 (see also Supplementary Table 2).

Code availability

The source code and software pipeline to reproduce our analyses can be assessed at <https://github.com/kotliary/baseline>.

References

41. van Lochem, E. G. et al. Immunophenotypic differentiation patterns of normal hematopoiesis in human bone marrow: reference patterns for age-related changes and disease-induced shifts. *Cytometry B Clin. Cytom.* **60**, 1–13 (2004).
42. Finak, G. et al. ImmuneSpaceR: A Thin Wrapper around the ImmuneSpace Database. <https://rdrr.io/bioc/ImmuneSpaceR/> (2014).
43. Bhattacharya, S. et al. ImmPort: disseminating data to the public for the future of immunology. *Immunol. Res.* **58**, 234–239 (2014).
44. Robin, X. et al. pROC: an open-source package for R and S+ to analyze and compare ROC curves. *BMC Bioinf.* **12**, 77 (2011).
45. Bates, D., Bolker, B. M., Maechler, M. & Walker, S. C. Fitting linear mixed-effects models using lme4. *J. Stat. Softw.* <https://doi.org/10.18637/jss.v067.i01> (2015).
46. Chaussabel, D. et al. A modular analysis framework for blood genomics studies: application to systemic lupus erythematosus. *Immunity* **29**, 150–164 (2008).
47. Weiner, J. tmmod: Feature Set Enrichment Analysis for Metabolomics and Transcriptomics. R package version 0.40 (2018); <https://CRAN.R-project.org/package=tmmod>
48. Benjamini, Y. & Hochberg, Y. Controlling the false discovery rate: a practical and powerful approach to multiple testing. *J. R. Stat. Soc. Ser. B* **57**, 289–300 (1995).
49. Choi, J. K., Yu, U., Kim, S. & Yoo, O. J. Combining multiple microarray studies and modeling interstudy variation. *Bioinformatics* **19** (Suppl. 1), i84–i90 (2003).
50. Subramanian, A. et al. Gene set enrichment analysis: a knowledge-based approach for interpreting genome-wide expression profiles. *Proc. Natl Acad. Sci. USA* **102**, 15545–15550 (2005).
51. Dobin, A. et al. STAR: ultrafast universal RNA-seq aligner. *Bioinformatics* **29**, 15–21 (2013).
52. Love, M. I., Huber, W. & Anders, S. Moderated estimation of fold change and dispersion for RNA-seq data with DESeq2. *Genome Biol.* **15**, 550 (2014).
53. Wickham, H. *ggplot2: Elegant Graphics for Data Analysis* (Springer-Verlag, 2016).
54. Torchiano, M. effsize: Efficient Effect Size Computation. R package version 0.7.6 (2019); <https://CRAN.R-project.org/package=effsize>
55. Wang, X. et al. An R package suite for microarray meta-analysis in quality control, differentially expressed gene analysis and pathway enrichment detection. *Bioinformatics* **28**, 2534–2536 (2012).
56. Seshan, V. clinfun: Clinical Trial Design and Data Analysis Functions. R package version 1.0.15 (2018); <https://CRAN.R-project.org/package=clinfun>
57. Yan, Y. MLmetrics: Machine Learning Evaluation Metrics. R package version 1.1.1 (2016); <https://CRAN.R-project.org/package=MLmetrics>
58. Stoeckius, M. et al. Cell Hashing with barcoded antibodies enables multiplexing and doublet detection for single cell genomics. *Genome Biol.* **19**, 224 (2018).
59. Stoeckius, M. et al. CITE-seq protocols (2017); <https://cite-seq.com/protocol>
60. Kang, H. M. et al. Multiplexed droplet single-cell RNA-sequencing using natural genetic variation. *Nat. Biotechnol.* **36**, 89–94 (2018).
61. Roelli, P. et al. Hoohm/CITE-seq-Count: 1.4.2. (Zenodo, 2019); <https://doi.org/10.5281/zenodo.2590196>
62. Lun, A. T. L. & Risso, D. SingleCellExperiment: S4 Classes for Single Cell Data. R package version 1.4.1. (2019); <https://bioconductor.org/packages/release/bioc/html/SingleCellExperiment.html>
63. Mule, M. P., Martins, A. J. & Tsang, J. S. Normalizing and denoising protein expression data from droplet-based single cell profiling. *bioRxiv* (in the press).
64. Ritchie, M. E. et al. limma powers differential expression analyses for RNA-seq and microarray studies. *Nucleic Acids Res.* **43**, e47 (2015).

65. Lun, A. T., Bach, K. & Marioni, J. C. Pooling across cells to normalize single-cell RNA sequencing data with many zero counts. *Genome Biol.* **17**, 75 (2016).
66. Waltman, L. & Eck, N. Jvan A smart local moving algorithm for large-scale modularity-based community detection. *Eur. Phys. J. B* **86**, 471 (2013).
67. Zappia, L. & Oshlack, A. Clustering trees: a visualization for evaluating clusterings at multiple resolutions. *GigaScience* **7**, giy083 (2018).
68. Pederson, T. L. ggraph: An Implementation of Grammar of Graphics for Graphs and Networks. R package version 1.0.2. (2018); <https://CRAN.R-project.org/package=ggraph>
69. Carlson, M. hgu95av2.db: Affymetrix Human Genome U95 Set annotation data (chip hgu95av2). R package version 3.2.3. (2016); <http://bioconductor.org/packages/release/data/annotation/html/hgu95av2.db.html>
70. Chen, J., Bardes, E. E., Aronow, B. J. & Jegga, A. G. ToppGene Suite for gene list enrichment analysis and candidate gene prioritization. *Nucleic Acids Res.* **37**, W305–W311 (2009).

Acknowledgements

We thank members of the Tsang Lab and the NIH Center for Human Immunology (CHI) for inputs and discussions; L. Failla for help with figures; D. Hirsch for testing the R code; and R. Germain and R. Apps for comments on the manuscript. This research was supported by the Intramural Research Program of the National Institute of Allergy and Infectious Diseases (NIAID) and Intramural Programs of the NIH Institutes supporting the Center for Human Immunology. Figure 6 was created with [BioRender.com](#).

Author contributions

J.S.T conceived and designed the study; R.S. and Y.K. collected and evaluated public datasets; Y.K., Y.L., A.J.M, M.P.M. and J.S.T designed data analysis strategies with inputs from R.S.; Y.K., Y.L., M.P.M. and A.J.M. performed data analysis with help from R.S., C.C.L. and F.C.; J.C. and P.L.S. contributed samples for CITE-seq; A.J.M, M.P.M. and N.B. developed protocols and generated CITE-seq data; M.G. and A.J.M. analyzed flow cytometry data prepared by A.B.; R.B. and V.P. provided SLE data; L.K. and S.M. sorted cells from healthy donors for RNA-seq analysis performed by A.J.M.; J.S.T. and R.S. wrote the manuscript with contributions from Y.K.; A.J.M., M.P.M. and Y.L. are co-second authors and contributed equally; J.S.T. supervised the study; all authors approved the manuscript.

Competing interests

The authors declare no competing interests.

Additional information

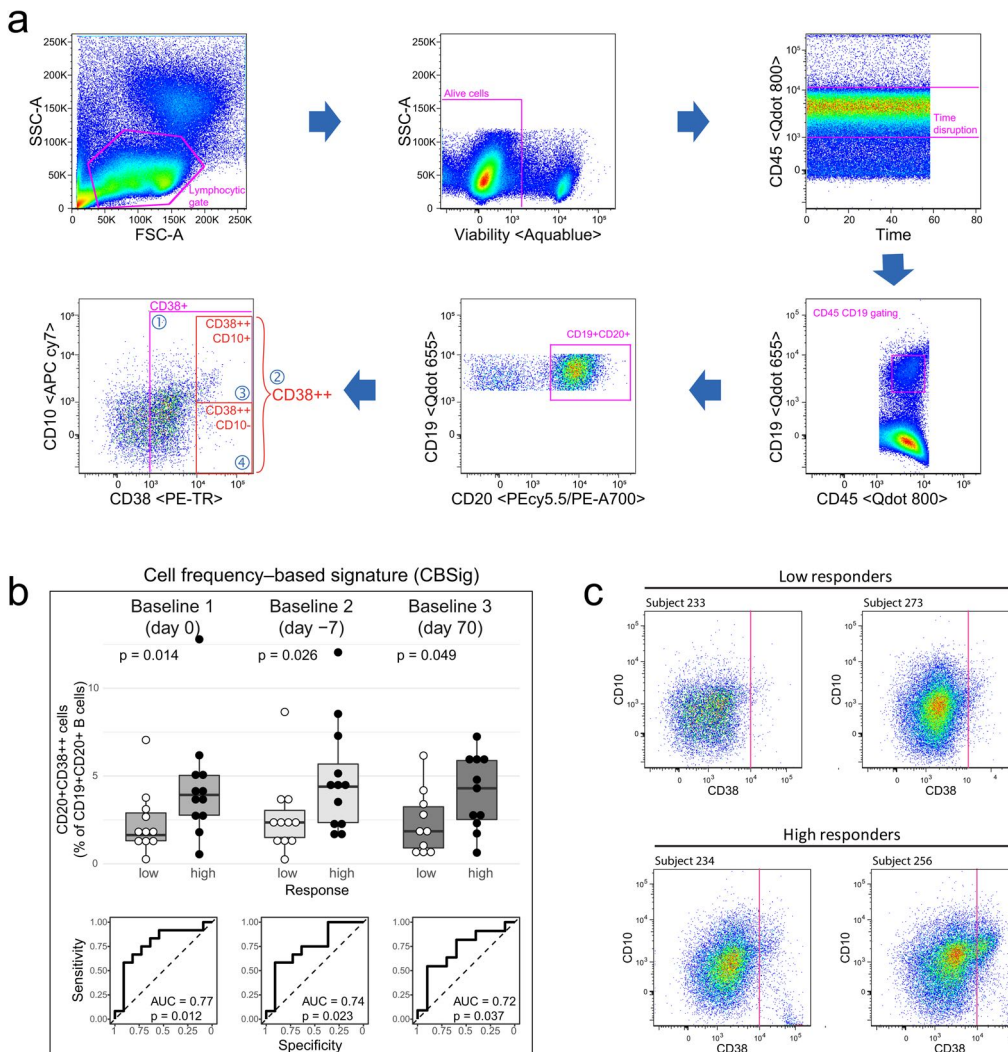
Extended data is available for this paper at <https://doi.org/10.1038/s41591-020-0769-8>.

Supplementary information is available for this paper at <https://doi.org/10.1038/s41591-020-0769-8>.

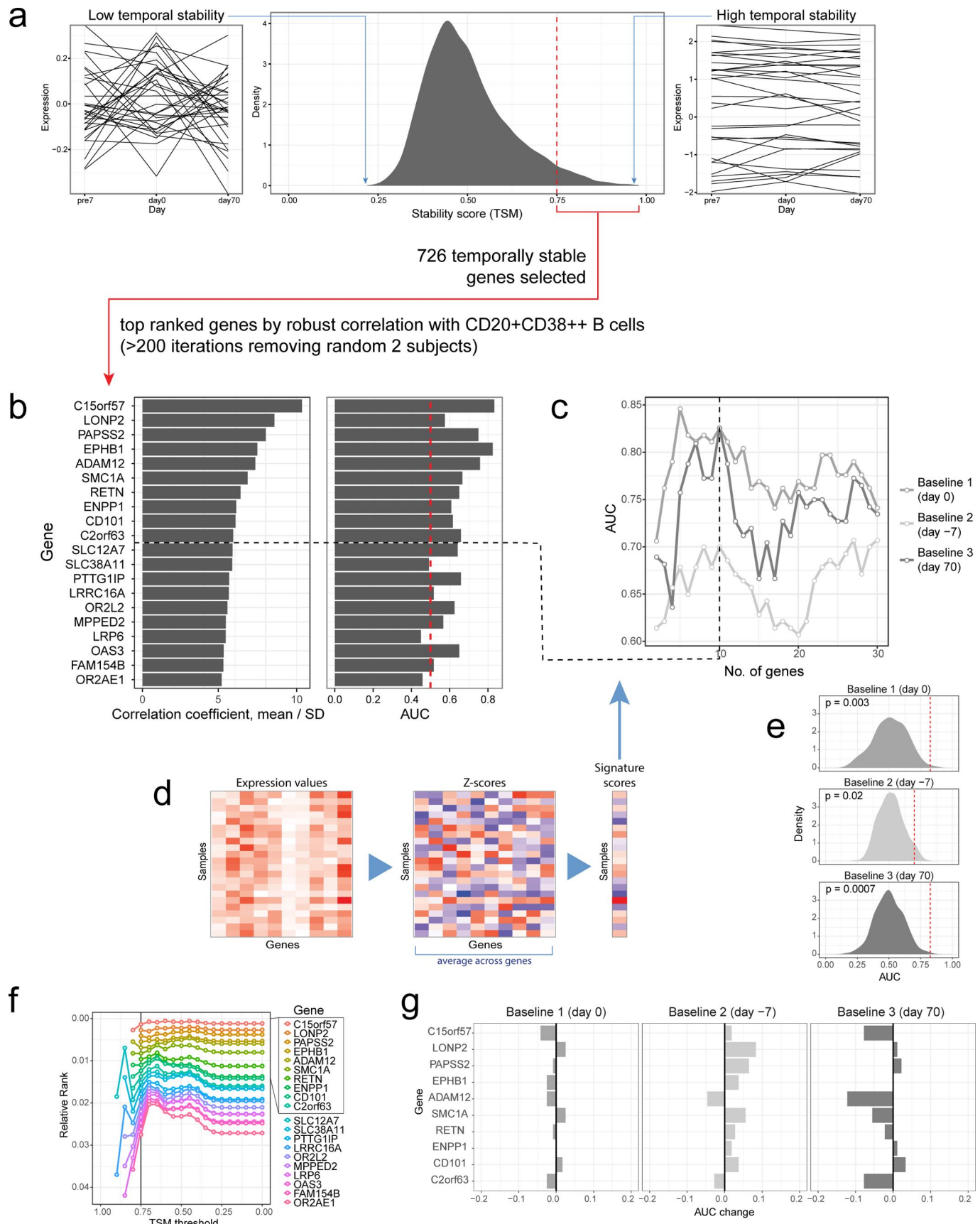
Correspondence and requests for materials should be addressed to J.S.T.

Peer review information Saheli Sadanand was the primary editor on this article and managed its editorial process in collaboration with the rest of the editorial team.

Reprints and permissions information is available at [www.nature.com/reprints](#).

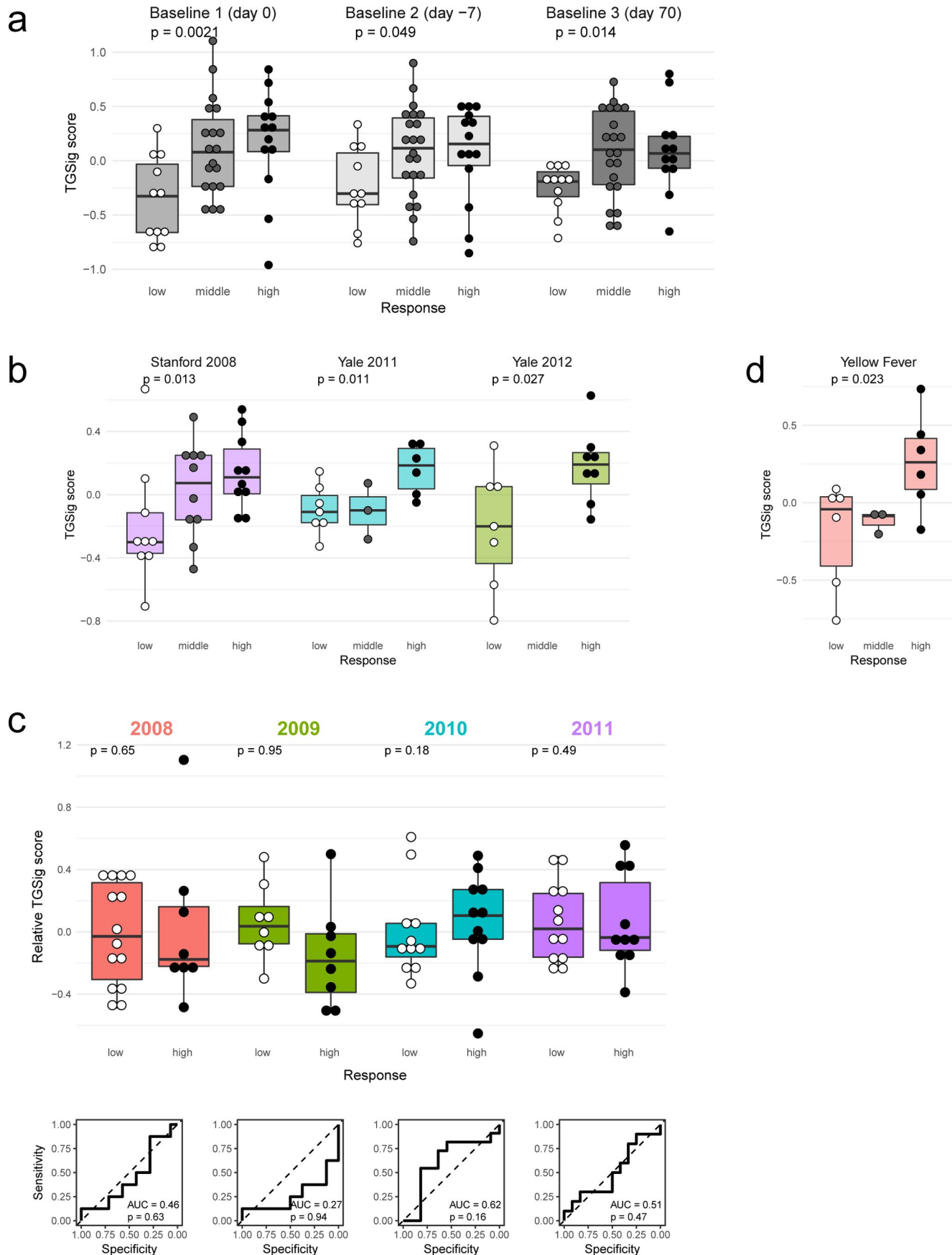


Extended Data Fig. 1 | Identification and characterization of the CD19+CD20+CD38++B cell population, a baseline, pre-vaccination cell frequency-based signature (CBSig) of antibody responses to influenza vaccination. **a**, Flow cytometric gating strategy for the CD19+CD20+CD38++ B cell population. Populations 1–4 are further described in (Fig. 1b). **b**, Box plots (top) showing the frequency of CD19+CD20+CD38++ cells (CBSig; y axis) at the three baseline time points from ref. ¹² (days −7 and 0 are prior to vaccination and day 70 is after vaccination) in low and high responders (x axis) to the seasonal and pandemic H1N1 influenza vaccines as defined by the Adjusted Maximum Fold Change (adjMFC) metric (see ref. ¹²). There are 11 low and 12 high responders for day −7 and 0, and 10 low and 11 high responders for day 70. P values from the Wilcoxon one-tailed test results are shown on the box plots (based on results from ref. ¹²; our hypothesis was that the high responders have higher frequencies of these cells than low responders). Boxplots' center line corresponds to the median value, lower and upper hinges correspond to the first and third quartiles (the 25th and 75th percentiles); lower and upper whiskers extend from the box to the smallest or largest value correspondingly, but no further than 1.5x inter-quartile range. (Bottom) Corresponding receiver operator curves (ROC) for vaccine response at each of the above baseline time points and their AUC (area under the curve) and corresponding permutation-based one-tailed p value are shown. **c**, Dot plots (CD38 vs. CD10 of CD19+CD20+B cells) for example high and low responders. **d**, Glossary of major abbreviations used in the study.



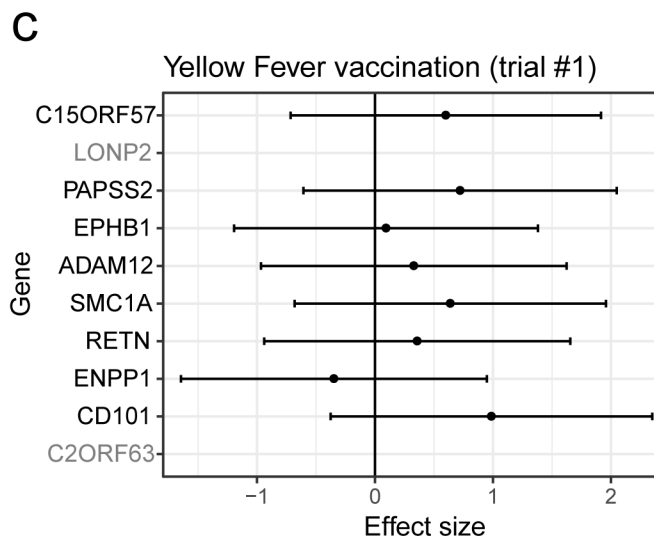
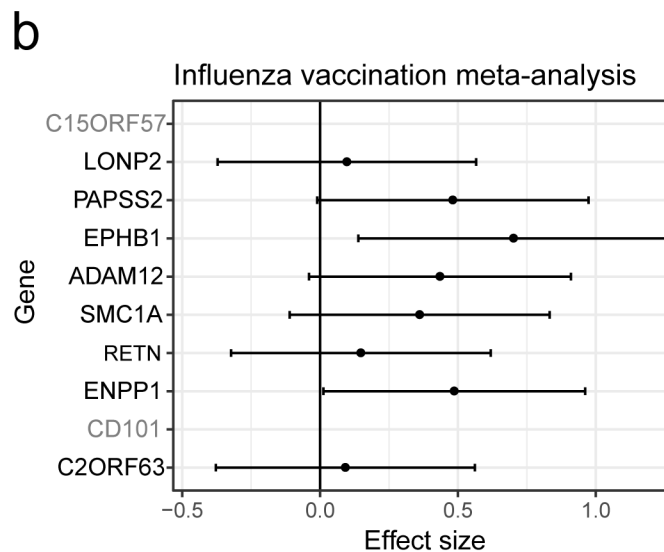
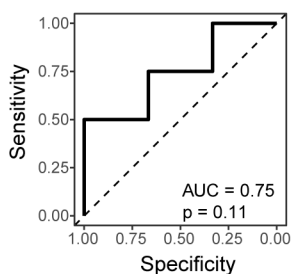
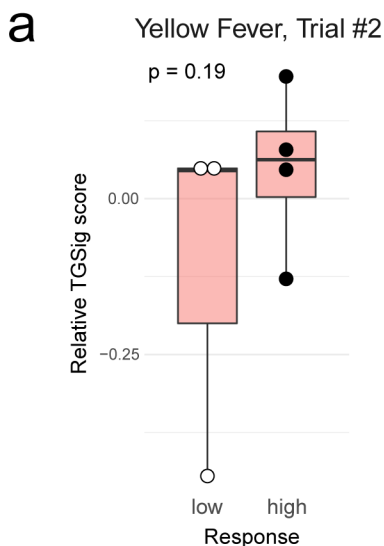
Extended Data Fig. 2 | See next page for caption.

Extended Data Fig. 2 | Derivation of TGSig, a transcriptional surrogate signature for CBSig. **a**, Step 1: Identification of genes with high temporal stability across the three baseline time points (days −7 and 0 are prior to vaccination and day 70 is after vaccination) in the NIH influenza study¹². The middle box shows the distribution of the temporal stability metric (TSM) across all the genes. The boxes on the right and left show examples of genes with high and low temporal stability, respectively; each line corresponds to an individual. Genes with high temporal stability (≥ 0.75) across the three baseline time points (depicted to the right of the red dashed line) were subsequently evaluated for correlation with CD19+CD20+CD38++ B cell frequency. **b**, Step 2: 726 temporally stable genes were ranked by their ‘robust’ correlation with CD19+CD20+CD38++ B cell frequency. Robustness is evaluated using all 231 random samplings of 20 subjects out of the cohort of 22 subjects (that is, two random subjects were dropped out from each sampling); the mean Spearman correlation coefficient divided by the standard deviation across the samplings (x axis left panel) was used to rank the genes. Top genes are shown together with the predictive performance of each gene evaluated at day 0 (AUC; right panel). The red dashed line in the right panel corresponds to AUC=0.50 (prediction performance as expected by chance); the top 10 genes were selected in TGSig (the black dashed line; see Supplementary Table 1 for full list of ranked genes) based on **(c)**. **c**, Performance (AUC; y axis) of the gene signature by baseline time point (different lines) and number of top genes included in computing the signature score (x axis). The vertical dashed line corresponds to a gene signature (TGSig) containing the top 10 genes achieving the best AUC across all three time points. **d**, Schema for gene signature score calculation. Gene expression data is standardized through calculation of Z-scores for each gene (that is, each gene would have mean 0 and standard deviation 1). The Z-scores for each gene in the signature are then averaged to generate the gene signature score. **e**, Distribution of predictive performance (AUC; x axis) of 500 random top-10 gene signatures generated from subject-label shuffled gene expression data using the robust correlation metric approach described above. The dashed red line indicates the observed AUC of TGSig at each of the baseline time points. One-tailed empirical p-values are shown. **f**, Relative rank (rank position divided by the total number of genes) of the top 20 genes from **(b)** and Supplementary Table 1 at different TSM thresholds. The black line shows TSM cutoff=0.75, the value used in selecting the top 10 genes for inclusion in TGSig (boxed). **g**, Change in AUC (x axis) of TGSig score following removal of the indicated gene in the signature (y axis) at each of the three baseline time points in the NIH influenza study.

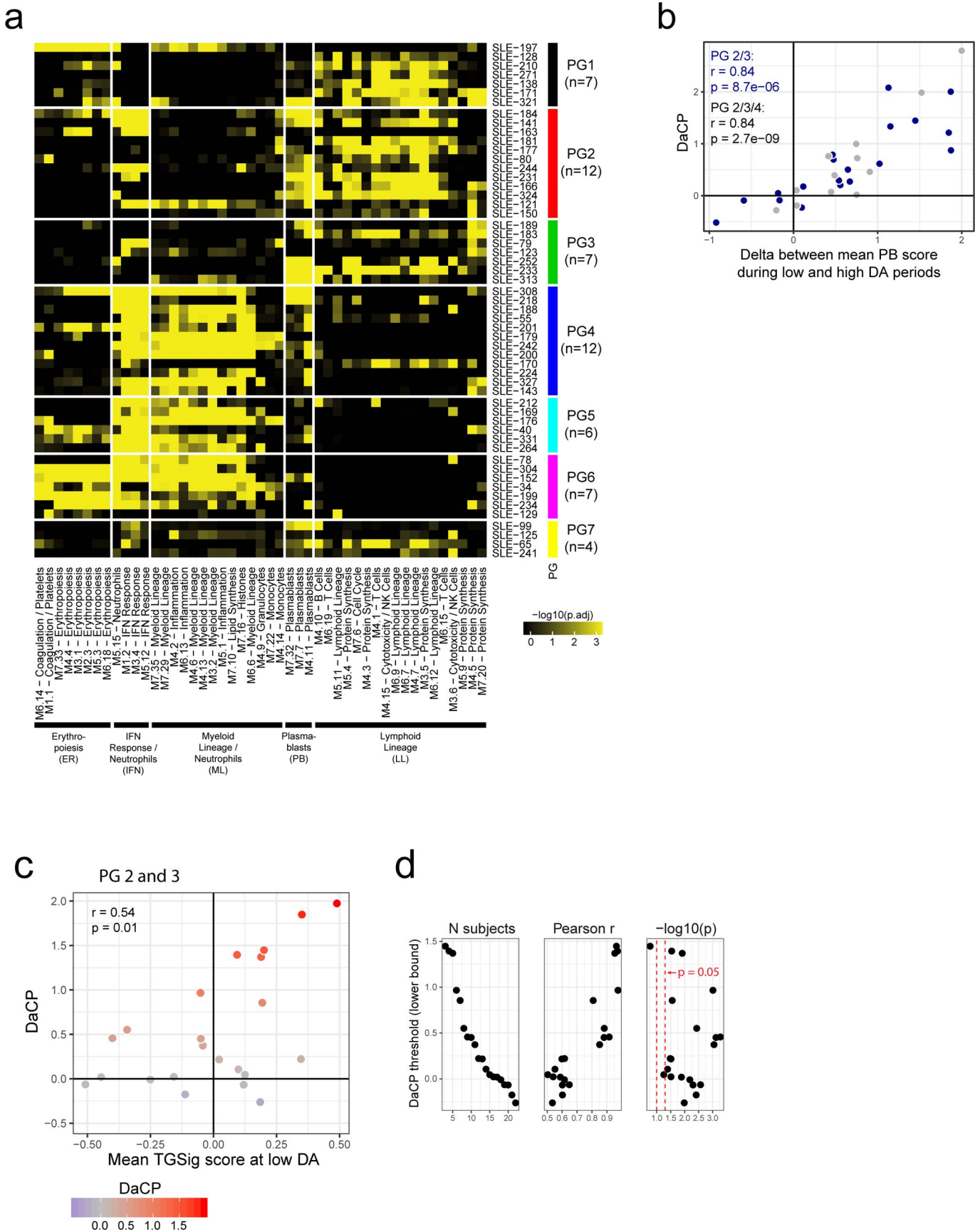


Extended Data Fig. 3 | See next page for caption.

Extended Data Fig. 3 | Comparison among response classes by including middle responders and evaluating TGSig in the influenza datasets from Emory¹⁸. **a**, similar to Fig. 1e, f but including middle responders (for day 0 n=11/19/13 for low/middle/high responders, respectively; for day -7 n=10/22/14 and for day 70 n=11/21/12); p values from the Jonckheere trend test (with an a priori alternative hypothesis that the high responders >= middle responders >= low responders.) For all box plots the center line corresponds to the median value, lower and upper hinges correspond to the first and third quartiles (the 25th and 75th percentiles); lower and upper whiskers extend from the box to the smallest or largest value correspondingly, but no further than 1.5x inter-quantile range. **b**, Similar to **(a)** but related to Fig. 2a; note that Yale 2012 does not have middle responders based on data retrieved from ImmuneSpace (n=9/10/10 (Stanford 2008), 7/3/6 (Yale 2010), 7/0/8 (Yale 2012)). **c**, Similar to Fig. 2a but testing TGSig using influenza datasets from Emory University over four years (n=14/8 low/high responders for year 2008, 8/8 for 2009, 11/11 for 2010, 12/10 for 2011). Box plots (top) showing the TGSig score (y axis) in low and high responders (x axis) as defined by adjMFC in the indicated season. P values shown on the box plots were obtained from the Wilcoxon one-tailed test. (bottom) Corresponding receiver operator curves (ROC) for vaccine response and the AUC (area under the curve) and corresponding permutation-based one-tailed p values are shown. **d**, Similar to **(a)** but for yellow fever and related to Fig. 2b.

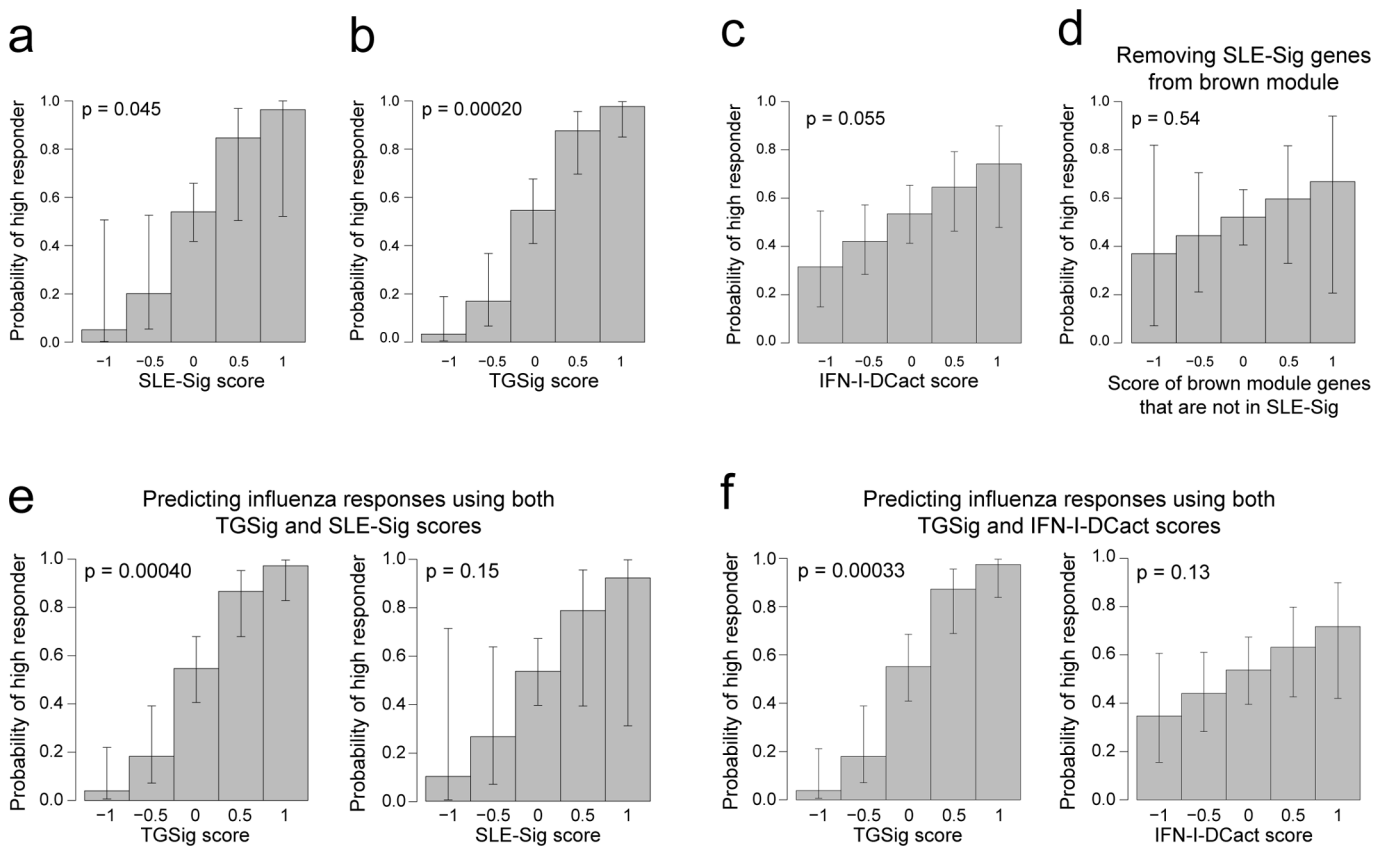


Extended Data Fig. 4 | Further evaluation of TGSig in yellow fever and influenza datasets. **a**, (top) Box plots (top) showing the TGSig score applied to pre-vaccination PBMC expression data (y axis) between low and high responders (x axis) to yellow fever vaccine in trial #2 (x axis; 4 high vs. 3 low responders). (bottom) Corresponding receiver operator curves (ROC) for vaccine response and the AUC (area under the curve) and corresponding one-tailed permutation-based p value are shown. This vaccination cohort included 10 subjects (see Fig. 2b for results on a first, larger trial with 15 subjects). Boxplots' center line corresponds to the median value, lower and upper hinges correspond to the first and third quartiles (the 25th and 75th percentiles); lower and upper whiskers extend from the box to the smallest or largest value correspondingly, but no further than 1.5x inter-quartile range. P-value is from Wilcoxon one-tailed test. **b**, Forest plot showing the meta-effect sizes (Hedge's g reflecting correlation strength with adjMFC) of the TGSig genes from a meta-analysis of four influenza datasets (Stanford 2008, NIH 2009, Yale 2011, Yale 2012; genes in gray were not present in all datasets); the bars represent the 95% CI. **c**, Similar to (b) but for yellow fever vaccination (computed from trial #1).



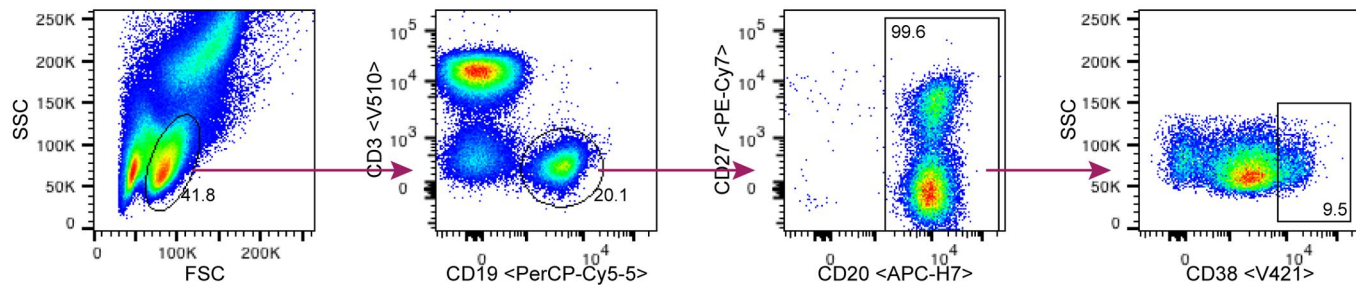
Extended Data Fig. 5 | See next page for caption.

Extended Data Fig. 5 | SLE patient phenotypes based on DA-associated transcriptional signatures and assessing the association between TGSig (at low DA) and DaCP after the removal of patients with lower DA-associated plasmablast signature scores. **a**, Recreation of Figure 6a from ref. ¹³ but as a robustness check here we used a different method: for each patient we ranked genes based on the difference between their average expression at high/middle and low DA time points and then performed GSEA analysis using the blood transcriptomic modules (columns) to fingerprint the patient. The colors on the heatmap denote the statistical significance (-log₁₀ of BH-adjusted p-values from CERNO³⁹) of the gene set enrichment test. Here we kept the order of patients (rows) and modules (columns) the same as in the original heatmap, although some patients from the original heatmap were removed due to the absence of low DA time points. The original patient groups were used to annotate the patients (rows). The overall fingerprinting pattern is visually highly consistent with the original heatmap. This heatmap/matrix was then used to construct Fig. 2c by averaging individual patient values within each patient and phenotype group combination. **b**, DaCP versus average plasmablast score difference between high (or middle if no high was available) and low DA time points in SLE patients from patient groups 2, 3 (in blue, n=19) or groups 2, 3, and 4 (group 4 in grey, n=12) from ref. ¹³ (see patient groups in Fig. 2c). Pearson correlation coefficients and two-tailed P values are shown. Spearman rho for groups 2 and 3 is 0.87 (two-tailed p = 2.2×10^{-16}); and for groups 2, 3 and 4 is 0.85 (two-tailed p = 4.9×10^{-7}). **c**, Similar to Fig. 2e, but here patients are from patient groups 2 and 3 only (n=22) and are shaded based on their DaCP. Note that there are more patients here for analysis from groups 2 and 3 than those shown in (a) and (b) because there we required that every patient has at least one low DA and one high/mid DA sample, while here (and in Fig. 2) the DaCP was estimated using all patients with at least one sample including those without high/mid DA time points (see Methods). Pearson correlation coefficient and two-tailed p values are shown. Spearman correlation coefficient is 0.47 (p = 0.029 two-tailed). **d**, Evaluating the correlation between DaCP and mean TGSig score at low DA time points (as in **c**) by removing patients with DaCP below the indicated cutoff (y axis). The first panel shows the number of patients in the evaluation given the threshold; the second and third panels show the corresponding Pearson r and two-tailed p value (shown as -log₁₀(p)).

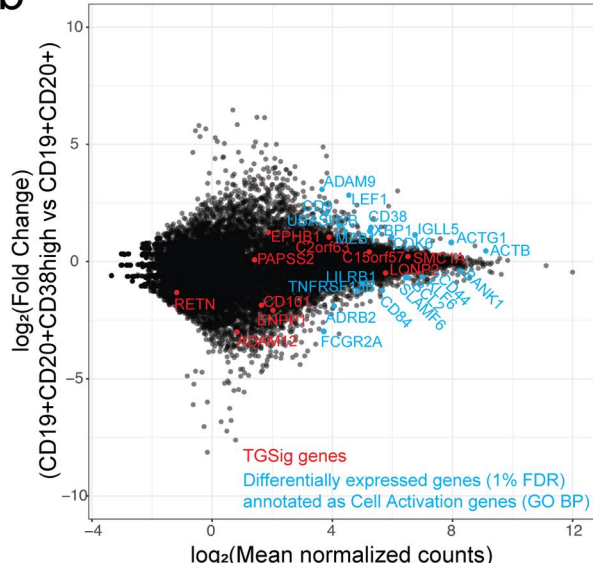


Extended Data Fig. 6 | Evaluating the predictive capacity and information overlap among the TGSig, SLE-Sig, and IFN-I-DCact signatures. **a-d**, The predictive profile of SLE-Sig (Fig. 3e) (a), TGSig (b), IFN-I-DCact (Fig. 3f) (c), and the non-leading edge genes from the brown module (Fig. 3e) (d) used as the sole predictor in logistic regression models of high versus low influenza vaccination responder status. Influenza vaccination data pooled from four datasets (Stanford 2008, NIH 2009, Yale 2011, Yale 2012) were used ($n = 71$ high and low responders). Note that for the brown module (Fig. 3a-d), most of the predictive information come from the leading-edge genes since the signature score of genes outside of the leading edge is not predictive (shown in d)). **e, f**, When both TGSig and SLE-Sig were used as predictors in the logistic regression (e) or when both TGSig and IFN-I-DCact score were used as predictors (f). In these graphs, the predictor scores are shown on the x axis and the probability that a high responder falls within the predictor score bin is shown on the y axis. The error bars correspond to 95% CIs. The two-tailed p value indicates the probability that the coefficient (“effect”) of the term (for example, TGSig score) in the logistic regression is 0.

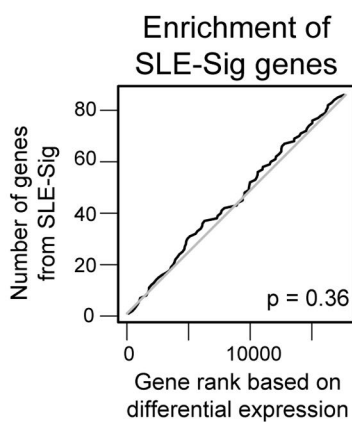
a



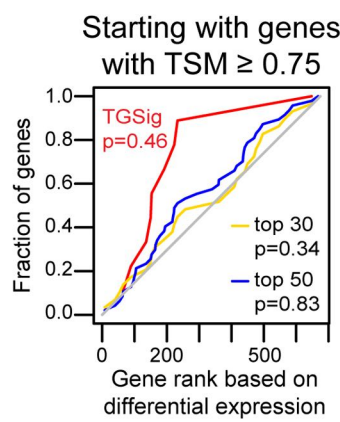
b



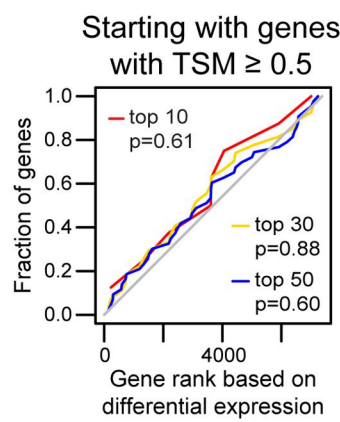
6



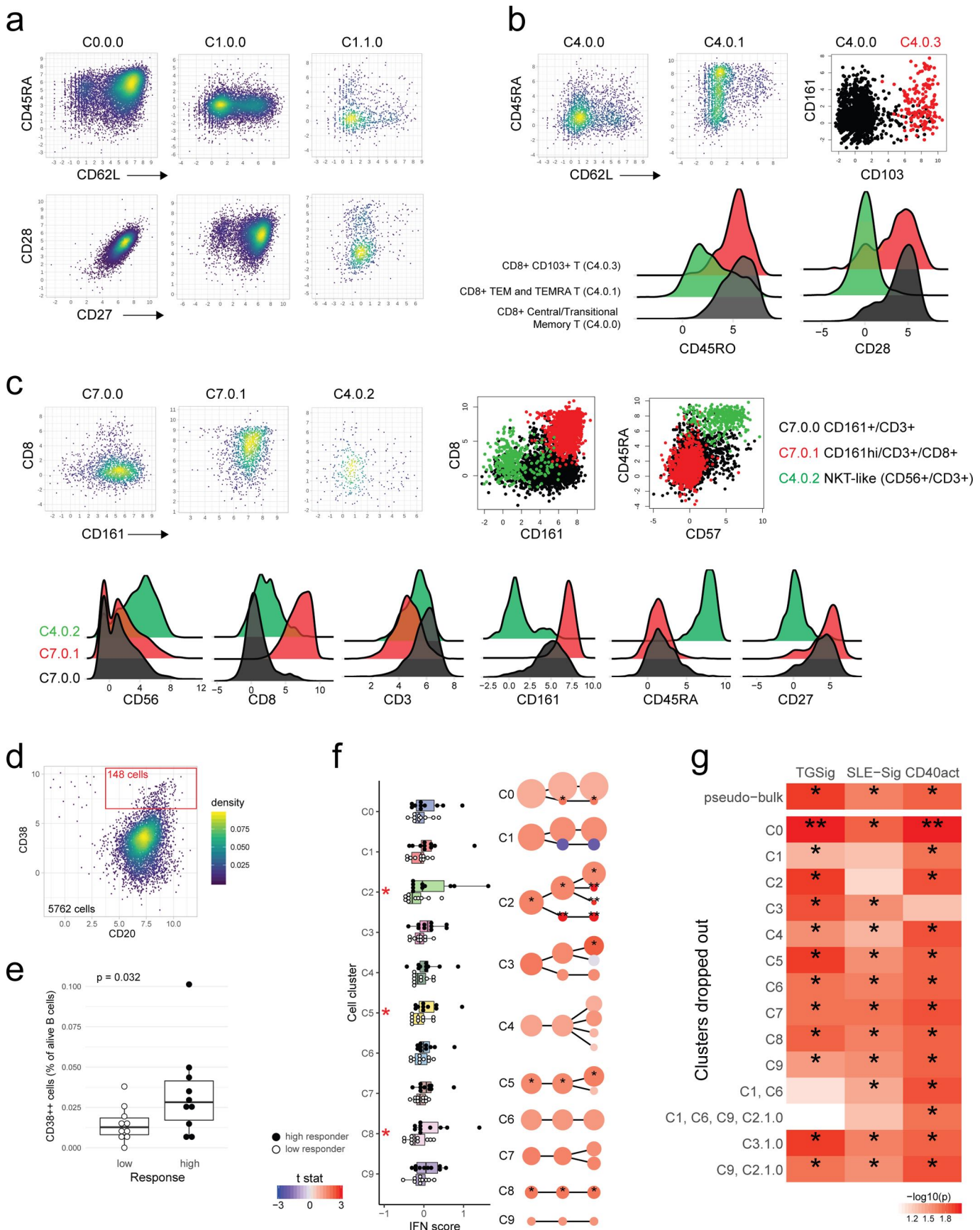
d



e

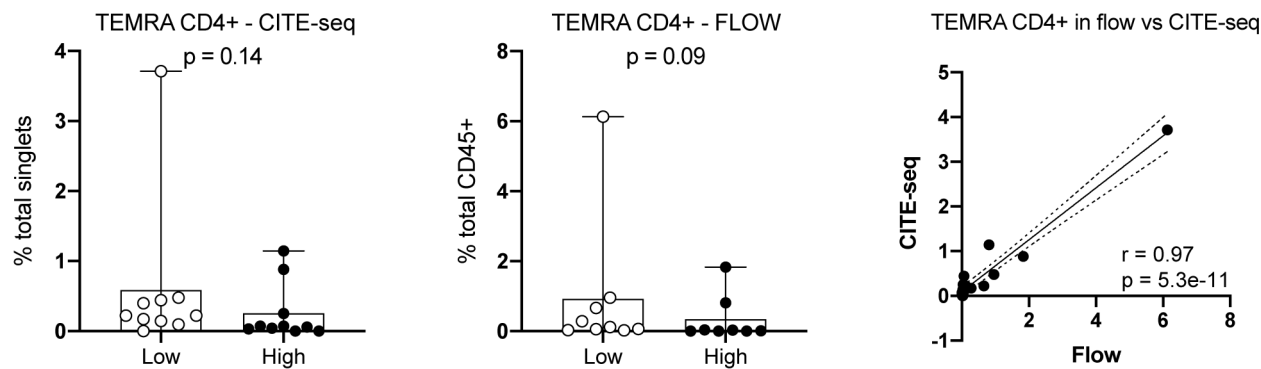
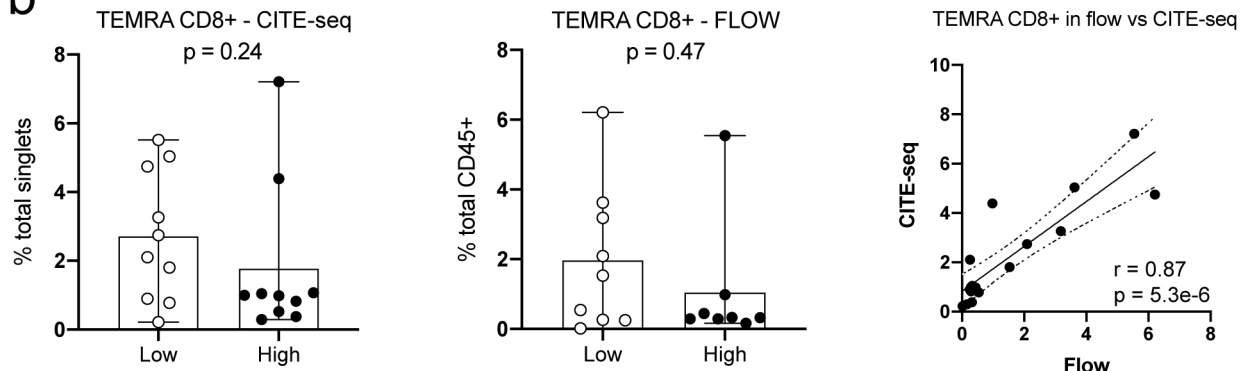
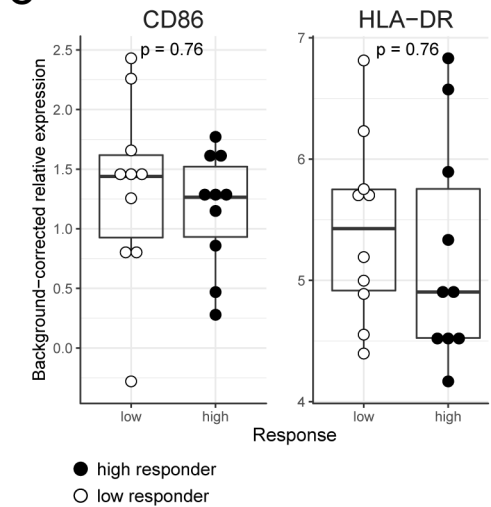


Extended Data Fig. 7 | RNA-seq analysis of CD19+CD20+CD38++ B cells sorted from healthy individuals. **a**, Sorting strategy and approach: CD19+CD20+ and CD20+CD38++ B cell populations were isolated by FACS from peripheral blood samples of six healthy donors. RNA-seq libraries were prepared for each isolated sample using the Nugen Ovation SoLo low-input RNA-seq library preparation kit. **b**, Differential gene expression between the CD20+CD38++ B cells and parental CD19+CD20+B cells from six paired samples was compared using DESeq2. Plot shows the log₂ fold change versus the log₂ of the mean normalized counts across all samples for each gene. TGSig genes are shown in red; genes from the differentially expressed gene set (BH-adjusted two-tailed p-value <1%, log of mean normalized counts >1; total genes in set: 105) that fall into the top enriched Gene Ontology Biological Processes category “Cell Activation” (enrichment analysis done using ToppGene⁷⁰) are shown in cyan (21 genes). **c**, Enrichment of the 87 SLE-Sig genes in genes ranked by differential expression between CD19+CD20+CD38++ versus CD19+CD20+ cells. The p value shown was computed from the GSEA test. **d**, Similar to **(c)** but instead of the SLE-Sig genes here the top k ($k=10$ (TGSig), 30, 50) genes correlated with the frequency of CD20+CD38++ B cells is assessed (only 713 temporally stable genes with $TSM \geq 0.75$ were included in the analysis); also see Extended Data Fig. 2. **e**, Similar to **(d)** but using 7731 genes with $TSM \geq 0.5$. A lower/more relaxed TSM cutoff was used to evaluate whether by starting with more genes (therefore potentially more statistical power for enrichment analysis) an enrichment signal can be detected.

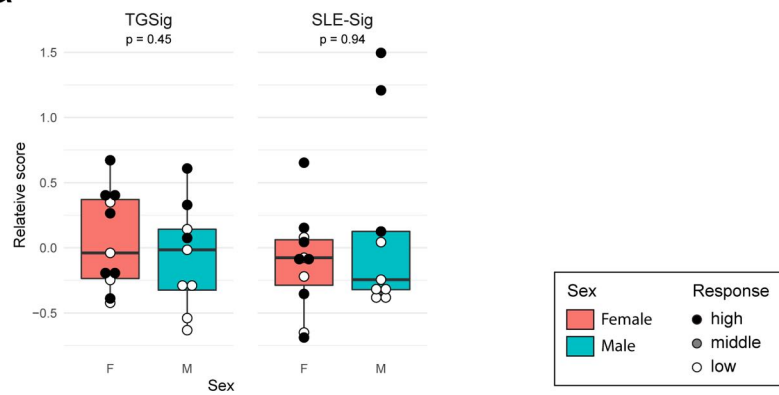
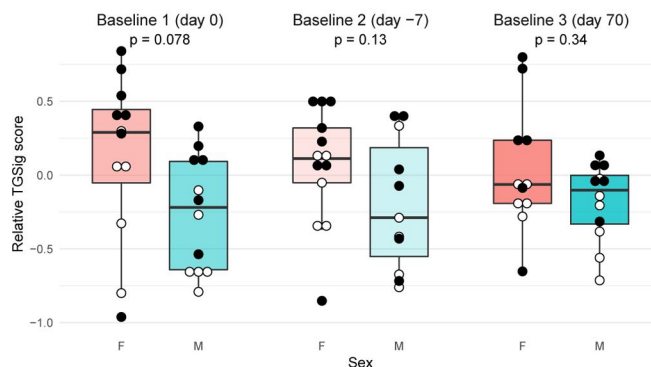
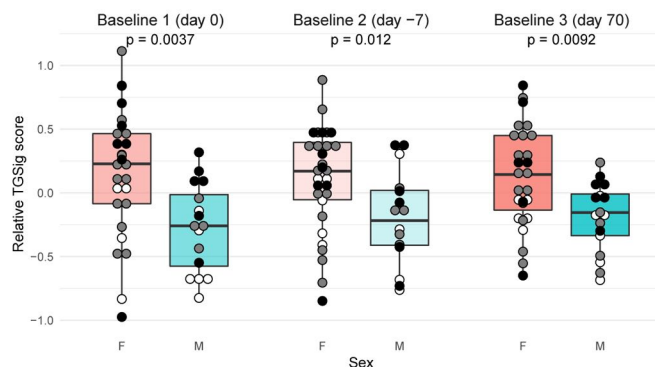
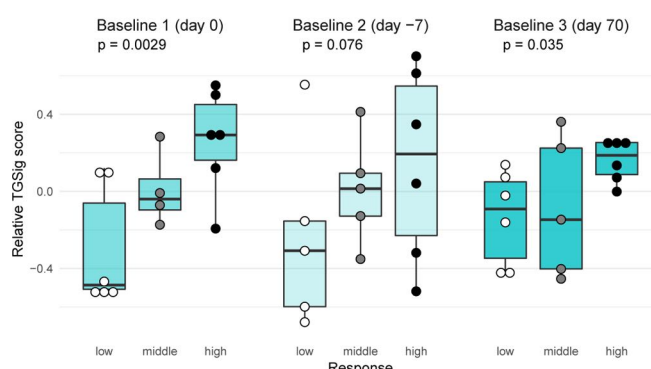
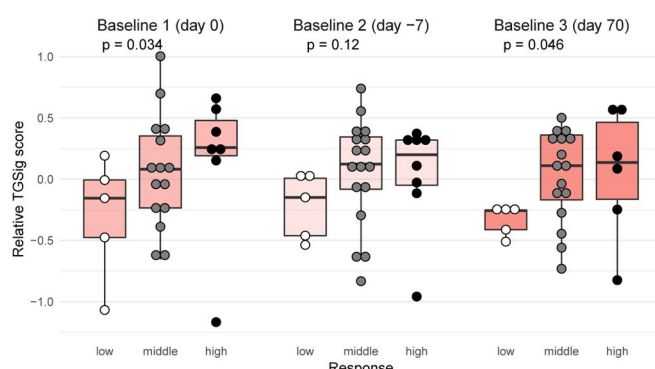


Extended Data Fig. 8 | See next page for caption.

Extended Data Fig. 8 | Supporting data for CITE-seq single cell analysis to dissect the cellular origin of baseline signatures. **a**, Single cell scatterplots of key markers in the CD4+T cell clusters. C0.0.0 (Naïve), C1.0.0 (Central/Transitional Memory), and C1.1.0 (TEMRA/Effector memory) clusters show different distributions of CD62L, CD45RA, CD27, and CD28. **b**, Distributions of key markers in the CD8+Memory T cell clusters. CD45RA vs. CD62L expression are shown in the top panels, ridge plots of CD45RO and CD28 are shown in lower panels. Similar to CD4+cells, these CD8+clusters show differences in CD62L and CD45RA distributions; C4.0.1 (TEMRA/Effector Memory) are mainly CD62L negative and CD28 negative, with CD45RA+(TEMRA) and CD45RO+(Effector Memory) subsets within this cluster. C4.0.0 and C4.0.3 show highly similar protein expression, with C4.0.3 being defined by high CD103 expression (upper right panel). **c**, Unconventional T cells (C7 clusters) show variable CD161, CD8, and CD56 expression. C7.0.0 and C7.0.1 are both CD3+/CD161+, with C7.0.1 being CD8 positive while C7.0.0 is CD8 negative. C4.0.2 (NKT-like) are also CD3 positive, but express CD57/56 and are CD8/CD161 negative or low. The C4.0.2 cluster also showed distinctly low CD27 and high in CD45RA compared to the C7 clusters, making it more similar to the C4.0.1 TEMRA/Effector memory CD8+subset, except expressing CD56/CD57; this could also be consistent with a Terminal Effector phenotype. **d**, Hand gating strategy for CD20+CD38++ B cells using CITE-seq data (number of cells in the gate shown in red). **e**, Boxplot comparing the hand gated frequency of CD20+CD38++ B cells between 10 high and 10 low responders; p value from Wilcoxon one-tailed test. Boxplots' center line corresponds to the median value, lower and upper hinges correspond to the first and third quartiles (the 25th and 75th percentiles); lower and upper whiskers extend from the box to the smallest or largest value correspondingly, but no further than 1.5x inter-quartile range. **f**, Similar to Fig. 5b (10 high versus 10 low responders) but for an independently obtained Type I IFN signature gene set (Supplementary Table 6: IFN gene set; see Methods). One or two asterisks denote significance with $p < 0.05$ or $p < 0.01$, respectively (Wilcoxon one-tailed test because we are interested in assessing whether the high responders are higher than the low responders; see also Supplementary Table 7). **g**, Results of the “drop out” analysis using CITE-seq data. The goal was to assess which cell clusters (or combination of clusters) that were individually significant delineators of high versus low responders were essential for prediction using the baseline signatures in bulk (i.e., simulating transcriptional data from PBMCs). The “pseudo bulk” results (average across all single cells for every subject in 10 low and 10 high responders) of the three signatures tested are shown on the first row. For subsequent rows cells from the indicated cell cluster(s) were dropped before repeating the pseudo-bulk analysis as in row 1. P values obtained from one-tailed Wilcoxon test: *: $p < 0.05$; **: $p < 0.01$.

a**b****c**

Extended Data Fig. 9 | Evaluating cytomegalovirus (CMV) correlates and pDC surface expression phenotypes strongly influenced by genetics from ref.³⁵
in high versus low responders. Since CMV status is not available for the cohorts we evaluated, we evaluated whether CMV correlates are significantly different between high and low responders in the NIH influenza vaccination cohort. **a**, Boxplots comparing the frequency of CD4+ TEMRA cells between 10 low and 10 high responders using CITE-seq (left panel) and between 9 low and 8 high responders using flow cytometry (center panel) data. Wilcoxon two-tailed p values are shown. The third panel is a scatter plot of CITE-seq versus the flow cytometry cell frequencies (n=17). Pearson correlation and two-tailed p values are shown. **b**, Same as (a) but for CD8+ TEMRA cells. **c**, Boxplots comparing the relative surface protein expression of CD86 and HLA-DR in pDCs (cluster C9) between 10 low and 10 high responders using CITE-seq data. Wilcoxon two-tailed p values are shown. For all box plots the center line corresponds to the median value, lower and upper hinges correspond to the first and third quartiles (the 25th and 75th percentiles); lower and upper whiskers extend from the box to the smallest or largest value correspondingly, but no further than 1.5x inter-quartile range.

a**b****c****d****e**

Extended Data Fig. 10 | Relationship between sex and baseline signatures. **a**, Box plots comparing the TGSig and SLE-Sig scores in females versus males; here only subjects with CITE-seq data are included to indicate that sex was not a driver of the differences between 10 high and 10 low responders emerged from CITE-seq data analysis (see Fig. 4). Wilcoxon two-tailed p values comparing 11 females and 9 males are shown. For all box plots the center line corresponds to the median value, lower and upper hinges correspond to the first and third quartiles (the 25th and 75th percentiles); lower and upper whiskers extend from the box to the smallest or largest value correspondingly, but no further than 1.5x inter-quartile range. **b**, Same as (a) but including all high and low responders from original NIH study¹². (day 0: 12 females and 12 males; day -7: 13 females and 11 males; day 70: 11 females and 12 males) **c**, same as (b) but including middle responders (i.e., all subjects in the study: day 0: 27 females and 16 males; day -7: 30 females and 16 males; day 70: 27 females and 17 males). **d**, Box plots comparing TGSig scores among low, middle, and high responders in males only (all subjects in the original NIH study used: day 0: 6/4/6 for low/middle/high responders, respectively; day -7: 5/5/6; day 70: 6/5/6). **e**, same as (d) but in females only (day 0: 5/15/17 for low/middle/high responders, respectively; day -7: 5/17/8; day 70: 5/16/6). All p values shown for two-group comparison were from the Wilcoxon two-tailed test; one-tailed p values shown for three-group comparison were from the Jonckheere trend test (with an a priori alternative hypothesis that the high responders >= middle responders >= low responders).

Reporting Summary

Nature Research wishes to improve the reproducibility of the work that we publish. This form provides structure for consistency and transparency in reporting. For further information on Nature Research policies, see [Authors & Referees](#) and the [Editorial Policy Checklist](#).

Statistical parameters

When statistical analyses are reported, confirm that the following items are present in the relevant location (e.g. figure legend, table legend, main text, or Methods section).

n/a Confirmed

- The exact sample size (n) for each experimental group/condition, given as a discrete number and unit of measurement
- An indication of whether measurements were taken from distinct samples or whether the same sample was measured repeatedly
- The statistical test(s) used AND whether they are one- or two-sided
Only common tests should be described solely by name; describe more complex techniques in the Methods section.
- A description of all covariates tested
- A description of any assumptions or corrections, such as tests of normality and adjustment for multiple comparisons
- A full description of the statistics including central tendency (e.g. means) or other basic estimates (e.g. regression coefficient) AND variation (e.g. standard deviation) or associated estimates of uncertainty (e.g. confidence intervals)
- For null hypothesis testing, the test statistic (e.g. F , t , r) with confidence intervals, effect sizes, degrees of freedom and P value noted
Give P values as exact values whenever suitable.
- For Bayesian analysis, information on the choice of priors and Markov chain Monte Carlo settings
- For hierarchical and complex designs, identification of the appropriate level for tests and full reporting of outcomes
- Estimates of effect sizes (e.g. Cohen's d , Pearson's r), indicating how they were calculated
- Clearly defined error bars
State explicitly what error bars represent (e.g. SD, SE, CI)

Our web collection on [statistics for biologists](#) may be useful.

Software and code

Policy information about [availability of computer code](#)

Data collection

The microarray data used were publicly available and can be accessed via NCBI GEO (see below also.) Titer data were publicly available and can be retrieved for the following data sets through ImmuneSpace and ImmPort: NIH (SDY80 and through <https://chi.niaid.nih.gov/> DATA/chi/09-H-0239/), Yale (SDY400, SDY404), Stanford (SDY212). The Emory antibody titer data was received via personal communications and can be found in the figshare site accompanying this paper (see link in the Data Availability section below). Flow cytometry data were previously reported in Tsang et al, Cell 2014 and this data was used to gate the additional cell populations (see Methods). CITE-seq data were generated using the protocol in the Methods, including using a 10x Genomics (Pleasanton, CA) workflow. RNA sequencing analysis was performed on sorted B cell populations derived from peripheral blood mononuclear cells of healthy human donors.

Data analysis

Full details of software versions can be found in Supplementary Table 8. Flow cytometry data was gated using FlowJo v9.9.3 for OS X. Data analysis for the first part of the study (Figs. 1-3 and Ext. Data Figs. 1-7) was performed using R version 3.4.1. CITE-seq data analysis was performed using R version 3.6.1. R packages from CRAN and Bioconductor repositories were used and their versions are listed in Supplementary Table 8. R code to reproduce the analysis is available at: <https://github.com/kotliary/baseline>. Software used for low-level processing of the CITE-seq data are listed in the "Computational low-level processing of CITE-seq data" section in Methods. Statistical analysis for Extended Data Fig. 9 was performed using GraphPad Prism version 8.3.0.328 (GraphPad Software, San Diego, CA).

For manuscripts utilizing custom algorithms or software that are central to the research but not yet described in published literature, software must be made available to editors/reviewers upon request. We strongly encourage code deposition in a community repository (e.g. GitHub). See the Nature Research [guidelines for submitting code & software](#) for further information.

Data

Policy information about [availability of data](#)

All manuscripts must include a [data availability statement](#). This statement should provide the following information, where applicable:

- Accession codes, unique identifiers, or web links for publicly available datasets
- A list of figures that have associated raw data
- A description of any restrictions on data availability

All data used in the study including the flow cytometry and CITE-seq data in analysis-ready format are available at figshare: <https://doi.org/10.35092/yhjc.c.4753772>. All microarray data were publicly available prior the study. Titer data was publicly available for the following data sets through ImmuneSpace and ImmPort: NIH (SDY80), Yale (SDY400, SDY404), Stanford (SDY212). The Emory antibody titer data was received via personal communications and can be found via the figshare link above. See Supplementary Table 2a for details. The original/raw public gene expression data are available in the National Center for Biotechnology Information Gene Expression Omnibus (GEO) under accession numbers: GSE47353, GSE41080, GSE59654, GSE59743, GSE29619, GSE74817, GSE13486, and GSE65391.

Field-specific reporting

Please select the best fit for your research. If you are not sure, read the appropriate sections before making your selection.

Life sciences Behavioural & social sciences Ecological, evolutionary & environmental sciences

For a reference copy of the document with all sections, see nature.com/authors/policies/ReportingSummary-flat.pdf

Life sciences study design

All studies must disclose on these points even when the disclosure is negative.

Sample size	Sample sizes for the data sets used are reported in Supplementary Table 2a. CITE-seq experiment was performed for 20 samples: 10 low and 10 high influenza vaccination responders (20 subjects in total). Gene expression of CD38 high B cell populations were assessed using 6 healthy donors not included in the influenza vaccination study. See Supplementary Table 9 for demographic information.
Data exclusions	All sample exclusions (due to QC or scientific reasons) were performed prior to data analysis (see Methods for details and reasons for the exclusion).
Replication	TGSig was assessed using independent data from multiple publicly available vaccination studies and in one SLE study (see manuscript for results), as well as technically replicated by the CITE-seq experiment.
Randomization	No randomization of subjects was performed in this study. The subjects were assigned to low, middle and high responder classes by analysis of the antibody response to vaccination (log fold-changes of post- vs. pre-vaccination titers, except for Yellow Fever where the initial titer readings were close to zero and we only assigned subjects based on the post-vaccination titers). SLE patients were assigned to patient groups by unsupervised analysis of their gene expression association with disease activity. SLE samples from multiple visits were categorized to low, middle and high disease activity according to the SLEDAI.
Blinding	The TGSig signature was developed using the NIH/CHI data only before we assessed it using other datasets. Similarly, signatures associated with disease activity were developed using only the SLE dataset first before they were assessed using vaccination data.

Reporting for specific materials, systems and methods

Materials & experimental systems

n/a	<input checked="" type="checkbox"/> Involved in the study <input type="checkbox"/> Unique biological materials <input type="checkbox"/> <input checked="" type="checkbox"/> Antibodies <input checked="" type="checkbox"/> Eukaryotic cell lines <input checked="" type="checkbox"/> Palaeontology <input checked="" type="checkbox"/> Animals and other organisms <input type="checkbox"/> <input checked="" type="checkbox"/> Human research participants
-----	---

Methods

n/a	<input checked="" type="checkbox"/> Involved in the study <input checked="" type="checkbox"/> ChIP-seq <input type="checkbox"/> <input checked="" type="checkbox"/> Flow cytometry <input checked="" type="checkbox"/> MRI-based neuroimaging
-----	--

Antibodies

Antibodies used	Antibodies from Biolegend were used in CITE-seq; please see Supplementary Table 10 for details. Antibodies used for flow sorting are described in the methods under heading "Sorting of B cell populations from healthy donors."
Validation	Quality control and reproducibility statements are available on the following Biolegend TotalSeq-A website: https://www.biolegend.com/en-us/quality-control https://www.biolegend.com/en-us/reproducibility

Human research participants

Policy information about [studies involving human research participants](#)

Population characteristics	PBMC samples for CITE-seq were acquired previously (see Tsang et al, Cell 2014). Age, gender and race/ethnicity information for all subjects is publicly available (See Supplementary Table 9). Cohort characteristics for the other public data we used can be found in the original publications (and some may also be available in NCBI GEO and NIAID ImmPort.) See also Supplementary Table 2a.
Recruitment	PBMC used for CITE-seq were collected prior to the study; see Tsang et al, Cell 2014 for details on the original NIH cohort. See also Supplementary Table 2a. For sorting of B cell populations from healthy donors, 6 healthy donors were recruited under IRB approved protocol NCT00001281 (See Supplementary Table 9).

Flow Cytometry

Plots

Confirm that:

- The axis labels state the marker and fluorochrome used (e.g. CD4-FITC).
- The axis scales are clearly visible. Include numbers along axes only for bottom left plot of group (a 'group' is an analysis of identical markers).
- All plots are contour plots with outliers or pseudocolor plots.
- A numerical value for number of cells or percentage (with statistics) is provided.

Methodology

Sample preparation	This study uses previously generated Flow Cytometry data. See the respective publications cited, including Tsang et al, Cell 2014.
Instrument	See the original publications cited, including Tsang et al. Cell, 2014.
Software	FlowJo ver.9.9.3 (Becton Dickinson Co., Ashland, OR) on Mac OS X; R version 3.4.1.
Cell population abundance	Cell frequencies are expressed as the percentage of the parent population.
Gating strategy	Using the flow cytometry data and predictive B cell populations defined in (Tsang et al., 2014), we gated four new cell subsets using the CD38 and CD10 markers) under the CD45+CD19+CD20+ live B-cell population (See Extended Data Fig. 1). Gate 1: CD38+ cells with CD38 (G610-A) fluorescent intensity over 1000; gate 2: CD38++ cells with fluorescent intensity over 10000; gate 3: CD38++CD10+ cells with CD10 (R780-A) fluorescent intensity over 1000; gate 4: CD38++CD10- cells with CD10 fluorescent intensity below 1000.

Tick this box to confirm that a figure exemplifying the gating strategy is provided in the Supplementary Information.